Deposition of phosphates in the Pabdeh Formation, Kangan anticline, southwest Iran: Implications for Rare Earth Element enrichment

Fatemeh Haddad

fahaddad230@gmail.com

Shahid Beheshti University

Mohammad Yazdi

Shahid Beheshti University

Khalegh Khoshnoodi

Nuclear Science and Technology Research Institute, Nuclear Fuel Cycle Research School

Mehrdad Behzadi

Shahid Beheshti University

Research Article

Keywords: Phosphate mineralization, carbonate fluorapatite, REE, Kangan anticline, Iran

Posted Date: September 11th, 2024

DOI: https://doi.org/10.21203/rs.3.rs-4908201/v1

Additional Declarations: No competing interests reported.

Version of Record: A version of this preprint was published at Environmental Earth Sciences on March 18th, 2025. See the published version at https://doi.org/10.1007/s12665-025-12125-3.

Deposition of phosphates in the Pabdeh Formation, Kangan anticline, southwest Iran: Implications for Rare Earth Element enrichment

Fatemeh Haddad[a*], Mohammad Yazdi[a], Khalegh Khoshnoodi[b], Mehrdad Behzadi[a]

[a]*Department of Geology, Faculty of Earth Sciences, Shahid Beheshti University, Tehran 1983969409, Iran*

[b]*Nuclear Science and Technology Research Institute, Nuclear Fuel Cycle Research School, Tehran, Iran*

Abstract

The Kangan anticline in the Folded Zagros Zone contains phosphate deposits enriched in trace metals. Field observations, petrography, X-Ray Diffraction, Scanning Electron Microscopy, and whole-rock geochemistry are used to determine the petrogenesis of this phosphate deposit, evaluate the mechanisms of deposition, and assess the implications for trace metal enrichment. Phosphatic layers are grainstone–packstone with microfossils and contain green glauconite. Carbonate rocks of the Early–Middle Eocene Pabdeh Formation host the phosphate units. Glauconite, calcite, and fluorapatite are the primary minerals of the marine sedimentary phosphate deposit in the Kangan anticline. Whole-rock compositions of phosphate layers indicate negligible clastic components and show enrichment in U and HREE. Limestone and pelagic limestone units in the Pabdeh Formation do not display enrichment of these elements. Carbonate fluorapatite is the host mineral for REEs and uranium. Cation substitution into carbonate fluorapatite is considered to be the main mechanism of trace element enrichment due to positive correlations between P_2O_5 and trace metals; ion adsorption did not play a crucial role in the metal enrichment in these phosphates. Strong negative Ce anomalies, slight positive Eu anomalies and low

ΣLREE/ΣHREE ratios of phosphate layers indicate enrichment of the HREE relative to their marine origin. The depositional environment of the phosphate units is interpreted as a basin margin carbonate ramp in the reduced and suboxic-to-anoxic zone that had low detrital input but occasionally high-energy erosional events. Ocean upwelling had an essential role in depositing the sandy glauconite-bearing phosphate layers.

Keywords: Phosphate mineralization, carbonate fluorapatite, REE, Kangan anticline, Iran

1. Introduction

Sedimentary phosphates or phosphorites are chemical sedimentary deposits with high concentrations of phosphorus (P); these rocks usually contain 18–20% phosphate minerals (mainly francolite (Ca_{10} (PO_4 CO_3) $F_{2–3}$)) (Daessle and Carriquiry, 2008; Dar, 2013). Francolite, also known as collophane, is a type of cryptocrystalline carbonate fluorapatite and is generally <1mm in size (Daessle and Carriqsuiry, 2008; Dar, 2013). Due to its crystalline structure, cation substitution typically occurs due to Ca exchange for U, Sr, and the Rare Earth Elements (REE); anion substitution of F for OH can cause F concentrations of F to reach 4 wt% in francolite (Tzifas et al., 2017). Consequently, carbonate fluorapatite compositions are highly variable (Baioumy, 2011). Due to enrichment of trace metals in francolite, phosphates are a potential source of metals of economic interest, including the REE and U (Zanin and Zamirailova, 2007; Dar, 2013; Christmann, 2014; Emsbo et al., 2015; Hein et al., 2016). Of these metals, the HREEs are particularly significant in renewable energy technologies and electronics (Humphries, 2010; Long et al., 2010; British Geological Survey, 2011; Kato et al., 2011).

Marine sedimentary phosphates have highly variable REE patterns (Shields and Stille, 2001); these variations are generally attributed to changes in the chemical composition and debris content related to their depositional environment as well as the composition and nature (e.g. redox, pH) of the seawater from which they precipitate (Picard et al., 2002; Nasrollahzadeh Saravi et al., 2015). These rocks also are enriched in U relative to most crustal rocks (Molnár et al., 2018). For example, the average concentration of uranium in modern continental phosphorites is 75 ppm (Baturin and Kochenov, 2001). High concentrations of U and Th can also create environmental concerns (Long et al., 2010). Changing precipitation conditions or seawater compositions combined with variable continental debris input results in variations in the concentrations of REE and U phosphorites (Ismael, 2002). However, factors such as surface weathering (Hannigan and Sholkovitz, 2001) and burial diagenesis (Shields and Stille, 2001) can modify the concentrations of U and REE in phosphate deposits. Therefore, understanding the petrogenesis and the post-depositional alteration of phosphate deposits is crucial for understanding their potential economic significance.

Although sedimentary phosphates span a large portion of the geological record (Precambrian to Holocene), the main periods of phosphate deposition occurred during the Precambrian and Cambrian periods in China, Russia, and Australia; during the Permian in North America; during the Jurassic and Early Cretaceous in Eastern Europe; from the Late Cretaceous to Eocene in the Middle East and North Africa; and, during the Miocene in southeastern North America (Van Kauwenbergh, 2010; Abed, 2013; Abed et al., 2016). The largest known accumulation of phosphorites (>70 billion tons of phosphate) is found in the state of Tethys (Jasinski, 2011; Abed et al., 2016). Phosphate deposits of the lower Paleocene-Oligocene Pabdeh Formation in the Kangan anticline of Iran are part of the Tethys phosphate state and represent an

opportunity to understand the deposition of phosphate layers and elucidate the factors that can lead to enrichment of REE and U in these rocks.

In this contribution, we document the distribution and abundance of REE and U in marine sedimentary phosphates of the Kangan anticline of the Pabdeh Formation of Iran. We use petrography, mineral composition analysis, and whole-rock major and trace element analysis to constrain the depositional environment of these phosphate layers and to understand the mechanisms that lead to enrichment of trace metals in these rocks.

2. Geological setting

The Folded Zagros sedimentary belt extends from Oman to the NW of Iran, Turkey, Iraq, and Syria (Fig. 1). The Folded Zagros Zone (FZZ) resulted from the closure of the Neotethys ocean and Cretaceous collision of the Eurasian (Irainian) plate with the Arabian plate.

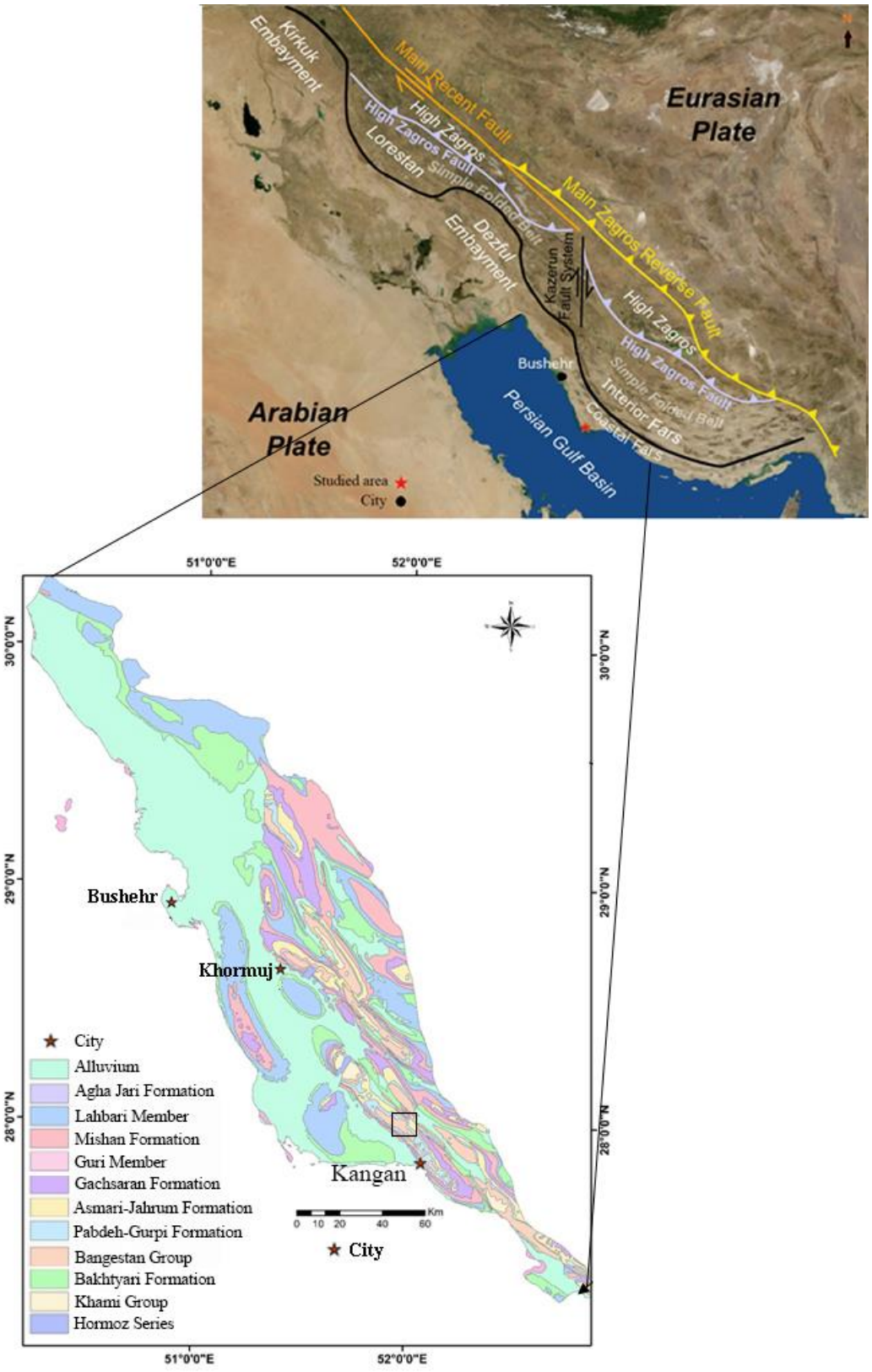

Figure 1. Generalized tectonic map of Iran (modified after File: ZagrosFTB.png." Wikimedia Commons) and the surrounding regions

The Zagros fold-thrust belt is divided into several zones based on sedimentary history and structural patterns. These zones include the Kirkuk Embayment, Lorestan, Dezful Embayment, and Fars (Interior and Coastal) (Fig. 1) (Abdulnaby, 2019; Aghanabati, 2004).

Various stages of the evolution of the Neotethys ocean are recorded in the FZZ; many of the rocks represent a typical carbonate platform that contains limestone, pelagic limestone and phosphates (Motiei, 2003; Heydari, 2008; Ahifar et al., 2015; Senemari and Foroghi, 2019).

The Cretaceous–Tertiary Pabdeh formation is exposed across the Zagros Fold Belt in southwestern Iran (Zarasvandi et al., 2021) in several anticlines, such as the Khormuj (Haddad et al., 2023) and the Kangan anticlines (this study). They are located in the coastal Fars zone. The distance between these two anticlines is ~100km. Both have almost similar stratigraphy and have whole-rock compositions. The Kangan anticline of SW Iran contains carbonate and phosphate units of the FZZ. The anticline has a width of ~10 km, a NW–SE trending fold axis, and extends along the coast of the Persian Gulf for 60 km. This anticline is exposed to the southeast of Bushehr city (Fig. 1). In this study, we focus on outcrops of the Kangan anticline to the northeast of the village of Darak (Fig. 2) where exposures allow detailed stratigraphic sections to be constructed that include phosphatic layers (Figs. 3, 4); Subsequently, compare the findings with the phosphate layers of the Khormuj Anticline (Haddad et al., 2023).

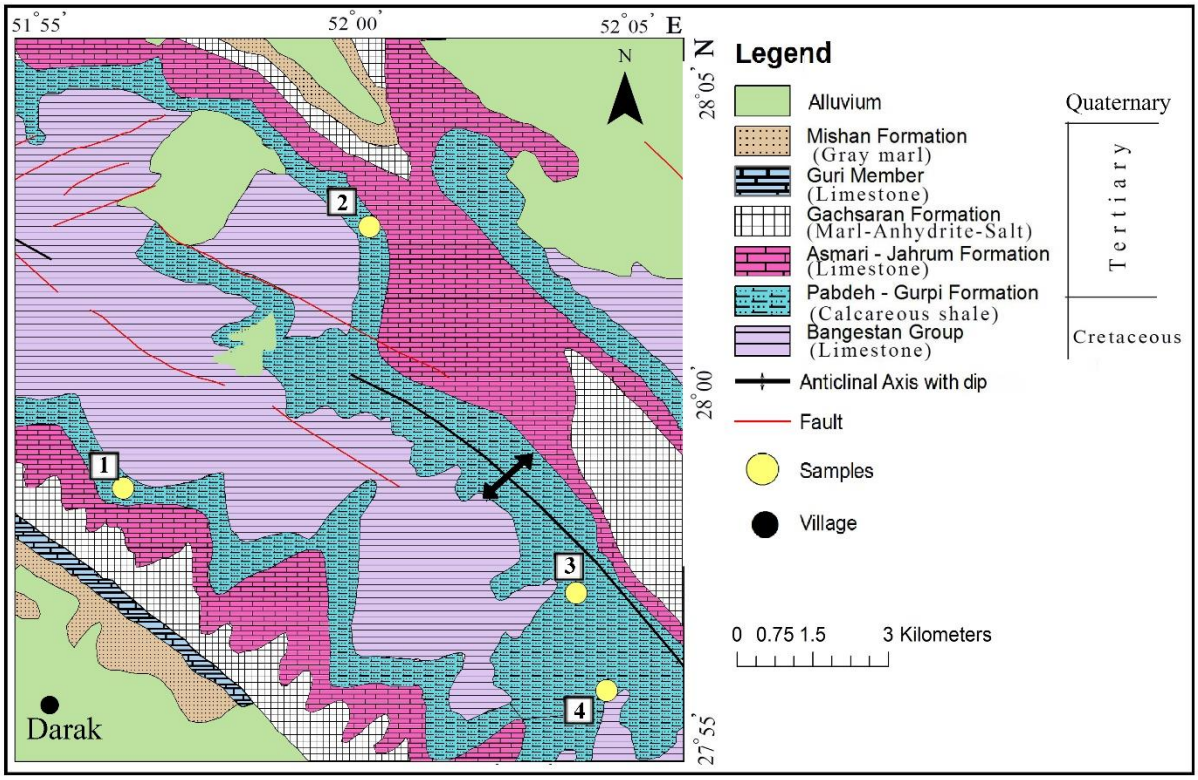

Figure 2. Simplified geological map (magnification of square of Fig. 1) and sample locations in the study area from the Kangan anticline

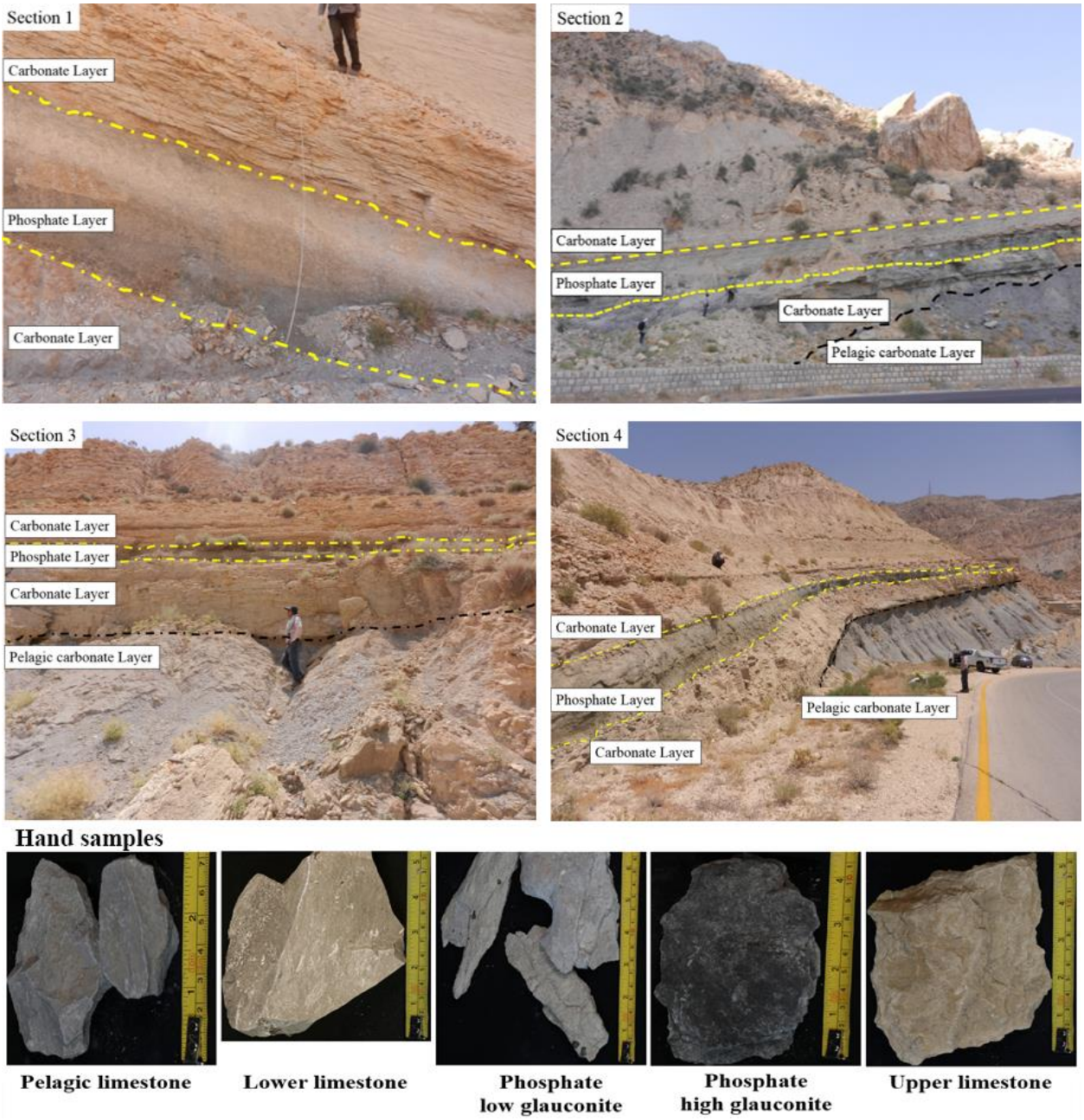

Figure 3. Sampling sections in the Kangan anticline accomplished hand samples taken from section 4. The thickness of the phosphate layer ranges from 1.80 m to 3 m.

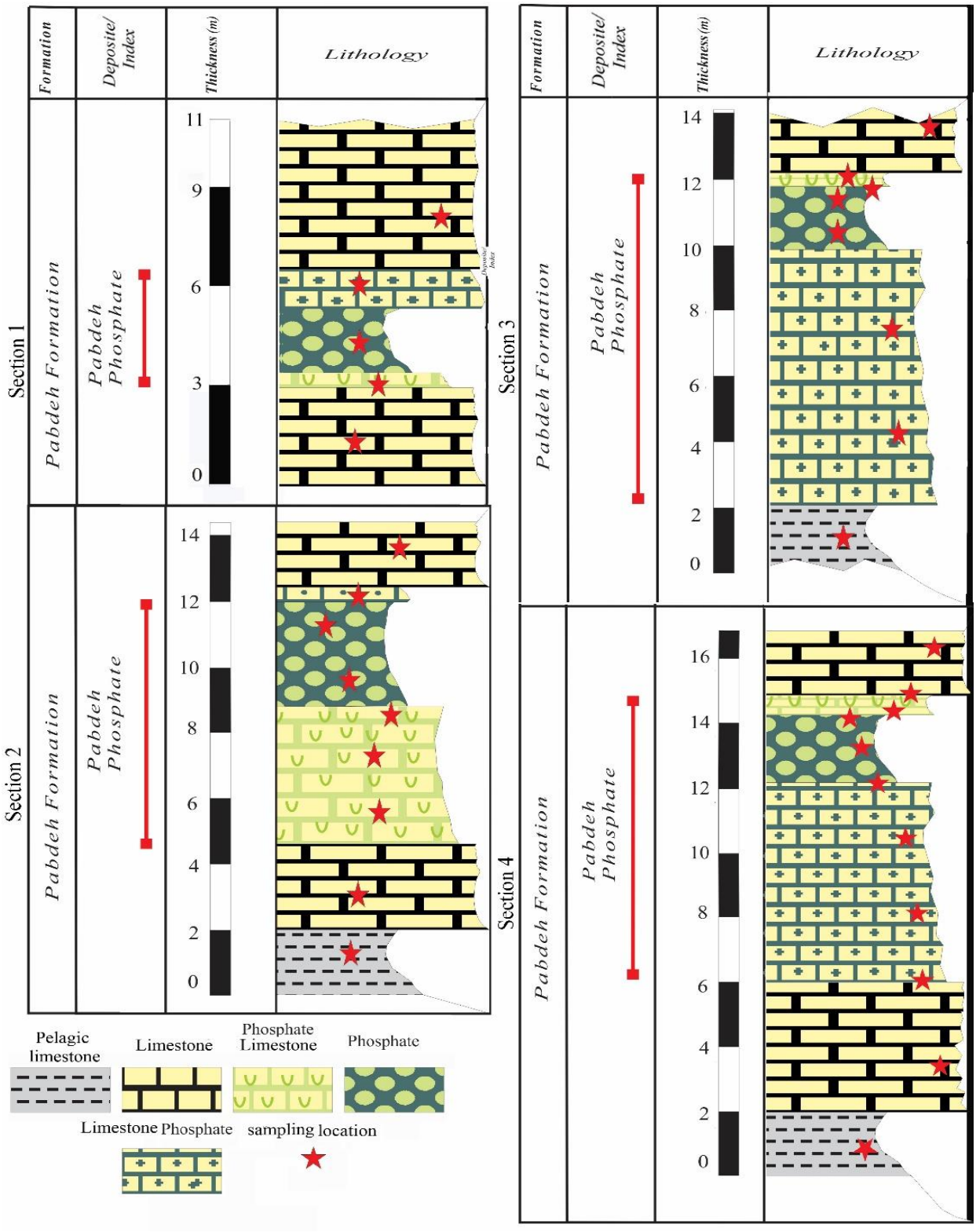

Figure. 4. Stratigraphic columns along with sampling locations from the Kangan anticline. Since the border between the layers is gradual, the amount of phosphate decreases gradually while the amount of limestone increases at the top and bottom of the phosphate layers. Based on the quantities of phosphate and limestone,

these sections have been named phosphate limestone (high phosphate) and limestone phosphate (high limestone).

The stratigraphy exposed in the Kangan anticline varies from Cretaceous to Quaternary. The oldest unit in the Kangan anticline is the Bangestan Group. The Cretaceous Bangestan Group is made up of the Razak, Sarvak, and Ilam limestone formations; these are covered by the Gurpi Formation (Early Maastrichtian- Late Paleocene), which is composed of marl, bluish-gray shale, with interbedded clay limestone. This is covered by the Early Eocene- Middle Eocene Pabdeh Limestone Shale Formation, which is an important phosphate-bearing formation in the region. The boundary between the Gurpi and Pabdeh Formations is gradational, and no sharp discontinuities are observed (Hadavi and Saboot, 2012). The Pabdeh Formation consists of marl, gray shale and marine clay limestone with green glauconite-bearing phosphatic layers. Nodular phosphatic layers of the Pabdeh Formation in Kangan anticline are surrounded by nodular limestone layers above and below (Fig. 3 and Fig. 4). The Pabdeh Formation is conformably overlain by marly limestone of the Early Tertiary Asmari–Jahrom Formation. The Asmari–Jahrom Formation is covered by Miocene evaporites (Gachsaran Formation) that include marl, anhydrite and salt. These evaporites are covered by early Miocene Guri member limestones. The Guri member (of the Mishan formation) is covered by the Early Miocene Mishan Formation and includes limestone, marly limestone and limestone marl. The Mishan Formation is overlain by Quaternary alluvial sediments (Fig. 2).

3. Sampling and Methods

Forty-one samples were collected from the four locations (Fig. 2) by systematic sampling (Figs 3, 4, and Appendix 1) perpendicular to the stratigraphic layering that included the pelagic

limestone, lower limestone, and sandy glauconite-bearing phosphate layers, and the upper limestone layers covering the phosphatic layer. The pelagic limestone layer was not exposed in section one; pelagic limestone samples were taken from the other sections. Phosphate limestone and Limestone Phosphate are low grade Phosphates. Samples were used to evaluate the mineralogical, petrographic, and geochemical characteristics of the phosphate, limestone and pelagic limestone units. Using transmitted and reflected microscopy, all samples were studied in thin sections to identify minerals and textures. Phosphatic layers were very hard and were sampled as chips from outcrops.

Appendix 1. The studied samples list from Kangan anticline Phosphates with the used methods

Samples			**Methods**				
Section	**ID**	**Features**	**A**	**B**	**C**	**D**	**E**
Section 1	Ka-1	Dark gray pelagic limestone, under the footwall	X				X
	Ka-2	Thin-bedded fresh limestone, footwall	X				X
	Ka-3	Phosphate	X				X
	Ka-4	Phosphate	X	X	X	X	X
	Ka-5	Phosphate	X				X
	Ka-8	Thin-bedded fresh limestone, hanging wall	X				X
Section 2	Ka-9	Dark gray pelagic limestone, under the footwall	X				X
	Ka-10	Thin-bedded fresh limestone, footwall	X				X
	Ka-11	Thin-bedded fresh limestone, footwall	X				X
	Ka-12	Phosphate	X				X
	Ka-13	Phosphate	X				X
	Ka-14	Phosphate	X				X
	Ka-15	Phosphate	X	X	X	X	X
	Ka-16	Phosphate	X				X
	Ka-17	Phosphate	X				X
	Ka-18	Thin-bedded weathered limestone, hanging wall	X				X

Section 3	Ka-19	Dark gray pelagic limestone, under the footwall	X				X
	Ka-21	Phosphate	X				X
	Ka-23	Phosphate	X	X			X
	Ka-24	Phosphate	X	X	X	X	X
	Ka-25	Phosphate	X				X
	Ka-26	Phosphate	X				X
	Ka-27	Phosphate	X				X
	Ka-28	Thin-bedded fresh limestone, hanging wall	X				X
Section 4	Ka-29	Dark gray pelagic limestone, under the footwall	X				X
	Ka-31	Thin-bedded fresh limestone, footwall	X				X
	Ka-32	Phosphate	X				X
	Ka-33	Phosphate	X				X
	Ka-34	Phosphate	X				X
	Ka-35	Phosphate	X	X			X
	Ka-36	Phosphate	X				X
	Ka-37	Phosphate	X		X	X	X
	Ka-38	Phosphate	X				X
	Ka-39	Phosphate	X				X
	Ka-40	Phosphate	X				X
	Ka-41	Thin-bedded fresh limestone, hanging wall	X				X

Legend: A. Petrographic microscope, B. X-Ray Diffraction (XRD), C. Scanning Electron Microscope equipped with Field Emission (FE-SEM), D. Scanning Electron Microscope equipped with Energy Dispersive X-ray Spectroscopy (SEM-EDX), E. Chemical analysis (ICP-Ms, ICP-OES)

X-Ray diffraction (XRD), field-emission Scanning Electron Microscopy (FE-SEM), and SEM Energy Dispersive X-ray spectroscopy (SEM-EDX) methods were used to characterize mineral compositions and microtextures. XRD was performed on five phosphate samples utilizing Cu Kα with an optic Monochromator 60kV/60mA, EQUINOX curved detector at the Applied Research Center of the country Geological Survey in Karaj, Iran. After covering with gold in the Applied Research Center of the Geological Survey, Karaj, Iran, polished thin sections of six

phosphate samples were investigated by FE-SEM (SIGMA/VP ZEISS model at 10 kV). Four phosphate samples were examined by an SEM-EDX model TESCAN-VEGA3 at 20 kV at the Materials and Metallurgical Engineering Department of Shiraz University, Iran. The specific analytical techniques applied to each sample are summarized in Appendix 1.

Four representative pelagic limestone samples, seven representative carbonates, twenty-five representative phosphate samples, were analyzed for rare earth elements (REE) and other trace metals (Y, Hf, Ga, U, and Th). The samples underwent preparation for analysis through a four-acid digestion method, which included the use of HCl, HF, HNO_3, and H_2SO_4 and analyzed by Inductively Coupled Plasma-Mass Spectrometry (ICP-MS) at the Applied Research Center of the Geological Survey, Karaj, Iran. Major element compositions and concentrations of select trace metals (Fe, Al, P, K, Ti, Na, Mg, Mn, Ca, Cu, Pb, Zn, V, Yb, Ni, Ba, Sr, Cr, Zr, and Nb) for twenty-five ore, seven carbonate, and four pelagic limestone samples were determined by Inductively Coupled Plasma-Optical Emission Spectrometry (ICP-OES) at the Applied Research Center of the Geological Survey (Karaj, Iran).

For calculating the quantities of the primary oxides including Al_2O_3, Fe_2O_3, P_2O_5, K_2O, TiO_2, Na_2O, MgO, and MnO the OXDPPM software (Al-Mishwat 2016) was employed. To conduct elemental analysis using ICP-MS and ICP-OES, the samples were prepared employing four acid digestion methods. These methods involved the use of HF, $HClO_4$, HCl, and HNO_3 as the digestion acids. In this particular approach, the procedure began by weighing 1 g of the dry sample and placing it into the crucible. Subsequently, 5 ml of concentrated HNO_3 was added to the crucible containing the sample. Following a 30-minute incubation period at room temperature, 10 ml of $HClO_4$ and 2 ml of concentrated HF were introduced to the sample in the crucible. Subsequently, the crucible, with its contents, was heated to 100°C. Following steeped in for 30

minutes at room temperature, 10 ml of $HClO_4$ and 2 ml of concentrated HF were introduced to the sample in the crucible. Subsequently, the crucible, with its contents, was heated to 100 $^{\circ}$C. Then the sample was left at the same temperature for 10 minutes, after the addition of 10 ml of HClO4 to make it clear. The sample was waited at room temperature until cooling, distilled water was then added to the sample until it reached a total volume of 50 ml and 100 ml flask. The analyses were executed after the digestion procedure, in accordance with the ASTM-D4698 method. To verify the accuracy of the results, replicate analyses were carried out. To verify the accuracy of the results, Certified Reference Materials (CRM) were used in the analysis procedure. As a result of the elevated Ca concentration exceeding 20 wt.% in the specimens, this particular element fell beyond the scope of the calibration's dynamic range, rendering it unmeasurable. Furthermore, in addition to this, while the four acids are being processed, a component of the Si in the samples is extracted in the form of vapor. By reason of, the quantity of Si contained in the samples could not be accurately ascertained.

4. Results

4.1 Petrography

Samples from the pelagic limestone layers, lower limestone layers, the sandy glauconite-bearing phosphate layers (base of the Pabdeh Formation), and the upper limestone layers covering the phosphatic layers were examined. Except for the lower pelagic limestone layers, all layers contain phosphatic nodules with microscopic to several centimeters size which are particularly relevant for exploration purposes (Bolourchifard et al., 2019).

4.1.1 Phosphatic layers

The phosphatic layers have a grainstone phosphorite texture, and contain phosphate grains such as pellets, ooids, intraclasts, vertebrates bone fragments, shells, teeth, and fish scales (biophosphate). Glauconite and clay minerals, quartz, pyrite, carbonate minerals (ankerite, and dolomite), iron oxide (hematite and goethite) and gypsum comprise the non-phosphate grains in these layers. Yellowish to dark brown pellets that lack internal structures are well rounded to semi-rounded and represent the most common phosphate type (Fig. 5a); these are composed of collophane. Phosphatic layers also contain oolites with concentric layers (Fig. 5b) and angular to rounded phosphate intraclasts (Fig. 5c). Organic matters (Fig. 5f) and some bioclasts, including fish teeth, bone, and skeletal fragments (Fig. 5d-e), have been wholly or partially phosphatized (Fig. 5f) or replaced with microcrystalline silica or dolomite/ ankerite (Fig. 5d-e). Glauconite is found in these layers (Fig. 5g-h-i and Fig. 7a-b). Aragonite and secondary rhombohedral dolomite and ankerite are numerous in phosphatic layers (Fig. 5j-d-e and Fig. 7cd-e). Framboidal and cubic pyrite was also observed (Fig. 6a-b-c-d and Fig. 7f). Some foraminifera chambers are partially filled by glauconite (Fig. 7g-h-i-j-k), apatite (Fig. 7h-i-l-k) and iron oxide (Fig. 5k and Fig.7c) (e.g. Pufahl et al. 2013, Rajabzadeh et al. 2017, Gál et al. 2020). Green chert (Fig. 5l) was also observed in different sizes (20-80 µm). Some gypsum (Fig. 6e-f and Fig. 7a-m) was also observed.

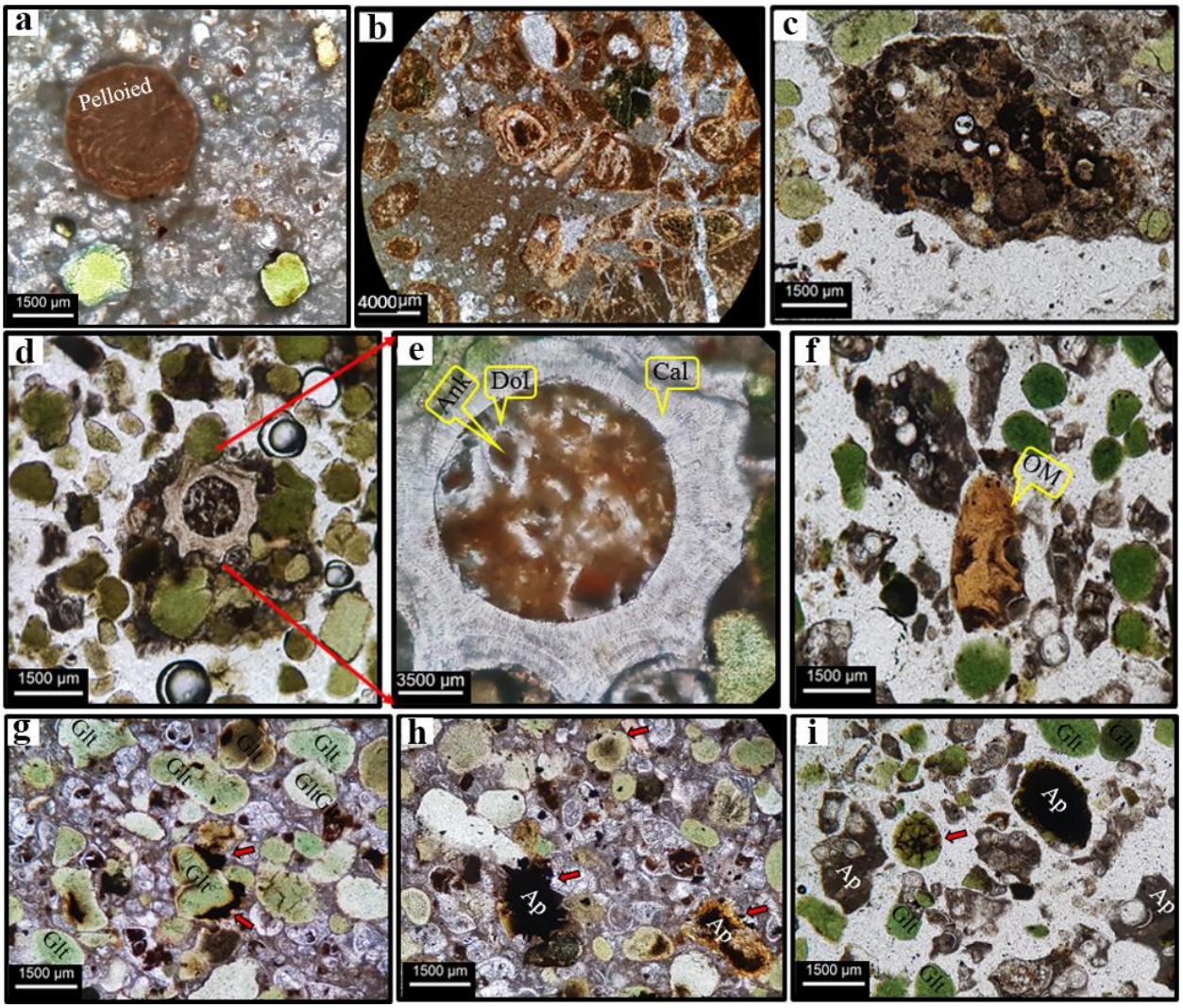

Figure 5. (a) Phosphatic pelloids in sandy glauconite-bearing phosphate layer. (b) Mono and multilayer ooids in the phosphate layer. (c) Phosphatic intraclast with phosphatization in microfossil chambers. (d) Dolomitization and ankeritization in a skeletal fragment. (e) Higher magnification of part of the image (d) showing ankerite surrounded by dolomite in the interior and surrounded by calcite. (f) Phosphatization on organic matter in sandy glauconite-bearing phosphate layer. (g) Phosphatization on the edge of glauconite grains. (h) Phosphatization in the center of glauconites. (i) Dendritic phosphatization in glauconite. (j) Dolomite crystal in the phosphate layer Mineral abbreviations. (k) Microfossil with phosphatic shell in phosphate mud; the chambers now composed of Fe-oxides. (l) Green chert in the phosphate layer. (m) Limestone layer with wackstone to packstone carbonate texture consisting of planktonic foraminifera in the micritic matrix with a benthic fossil and few glauconite grains. (n) Morozovella fossil with druze calcite cement in the limestone layer. (o) Pelagic limestone layer with a mudstone texture consisting of pelagic Foraminiferous silicic shells and strong laminations. Dol: Dolomite, Cal: Calcite, Ank: Ankerite, Glt: Glauconite, Cht: Chert, Ap: Apatite, OM: organic matter.

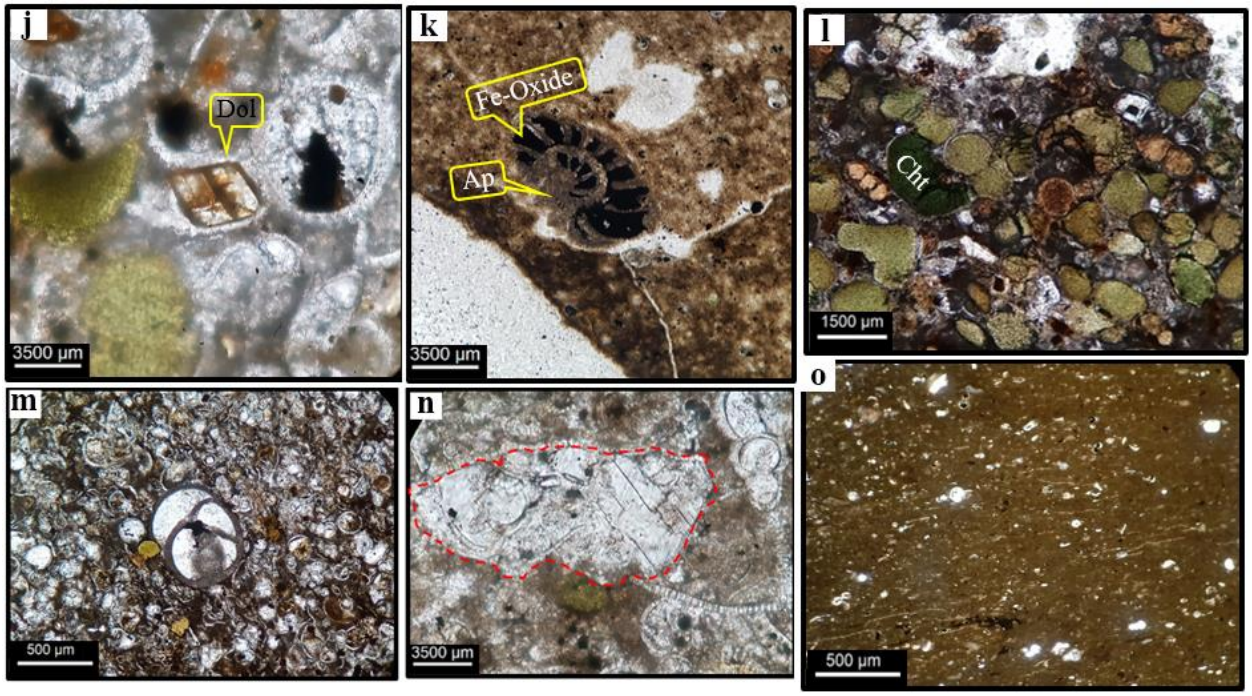

Figure 5. Continued.

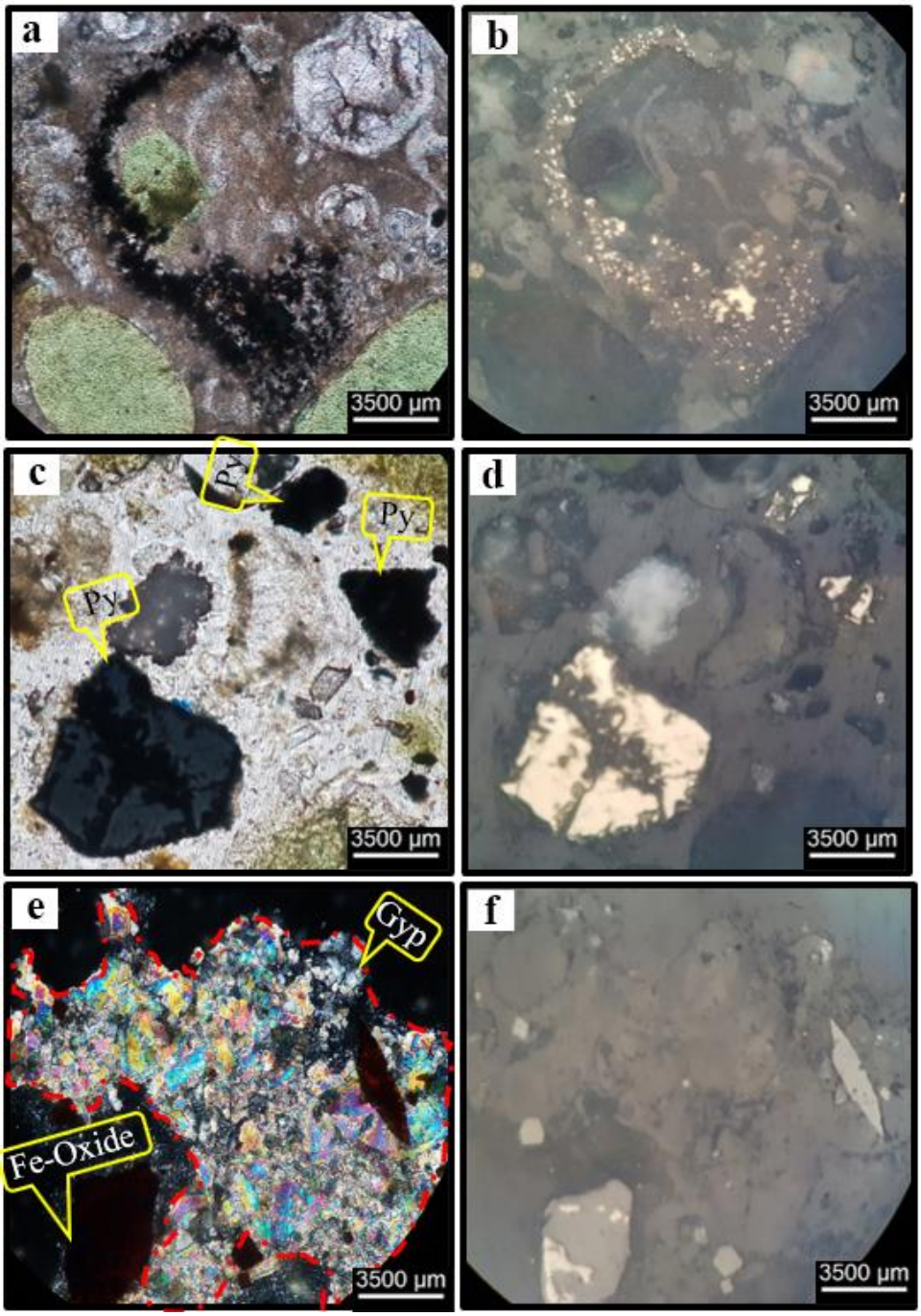

Figure 6. (a). Framboidal Pyrite in phosphate layer in transmitted light. (b) Reflective light image of (a). (c) Cubic pyrite in phosphate layer in transmitted light. (d) Reflective light image of (c). (e) Gypsum and Fe-oxide minerals in phosphate layer in transmitted light. (f) Reflective light image of (e).

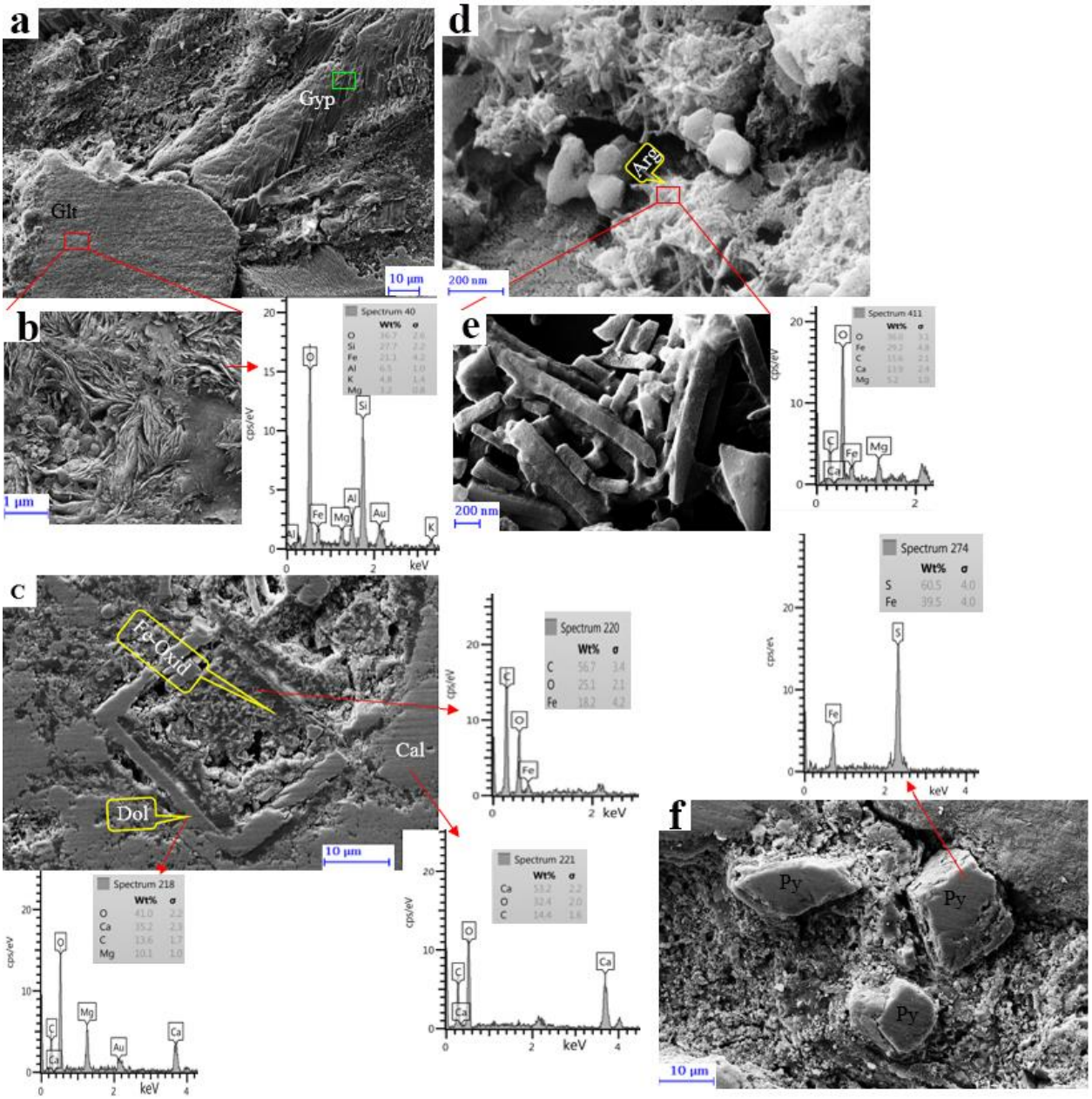

Figure. 7. Scanning electron microscope images and electron dispersive spectra of minerals in samples of phosphatic layer: (a) Gypsum (Gyp) and glauconite (Glt). (b) Higher magnification of part of the image (a). (c) Fe-Oxide, Dolomite (Dol) and Calcite (Cal). (d) Aragonite (Arg). (e) Higher magnification of part of the image (d). (f) Cubic pyrite (Py). (g) Foraminifera chambers filled with glauconite and its shell is made of calcite. (h) Quartz (Qtz), Foraminifera chambers filled with apatite and a glauconite the shell is made of calcite. (i) Higher magnification of part of the image (h) Hexagonal crystals of apatite. (j, k) Foraminifera chambers filled with apatite and glauconite. (l) Calcite foraminifera shell with a chamber filled with apatite. (m) Higher magnification of green square of the image (a). (n) The pyrite crystal replaced by Fe-Oxide.

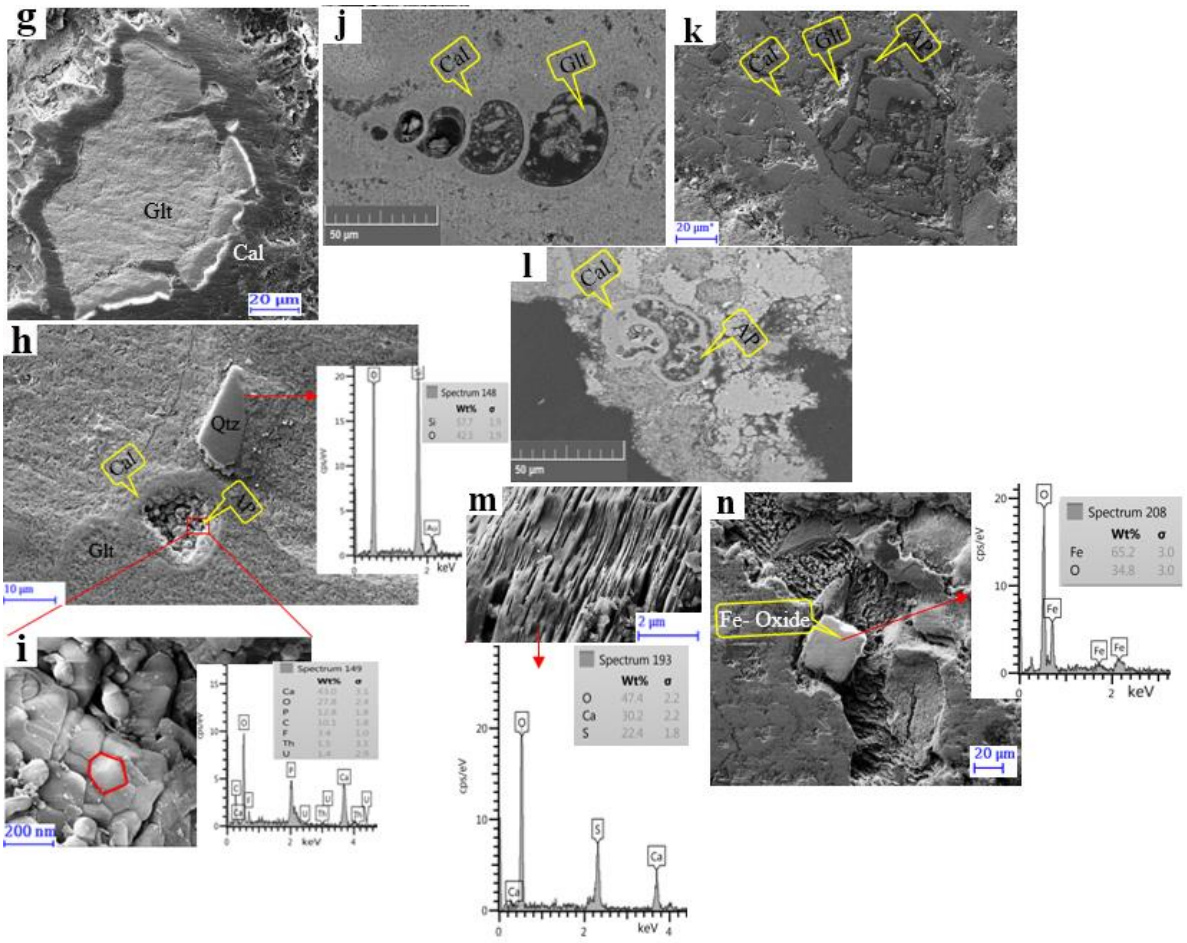

Figure. 7. Continued.

4.1.2 Limestone layers

Lower and upper limestone layers are wackstone to packstone carbonate containing benthos and plankton foraminiferal mats in a micritic matrix (Fig. 5m-n). More organic material is found in these layers relative to the phosphatic layers. Green glauconite (containing Fe^{2+}) is rare in limestone layers. In the lower limestone layers, *Morozovella, Conicotruncata Sp.* (lower Paleocene) (Fig. 5n), and other microfossils were replaced by calcite cement. Disseminated pyrite grains is also found in the limestone samples (Fig. 5n, yellow arrows).

4.1.3 Pelagic limestone layers

Pelagic limestone layers are dominated by calcareous oozes and some clay; it shows fine laminations (Fig. 5o) and contained carbonate and silica skeletal material of pelagic organisms.

4.2 Mineral compositions

XRD analyzed mineral components of five phosphate samples. For all samples, the main minerals include glauconite (mica–illite), calcite and carbonate fluorapatite (francolite); minor minerals include quartz, dolomite, ankerite, hematite, and gypsum. Orthoclase and siderite occur in trace amounts (Appendix 2). The presence of gypsum was also confirmed by petrographic study and SEM analysis (Fig. 6e, f and Fig. 7a, m). Based on the XRD data, the dominant clay mineral was the glauconite, and carbonate fluorapatite is the appropriate end-member of apatite.

Appendix 2. XRD analysis results.

Sample	Major minerals (>25%)	Minor mineral(s) (5–25%)	Trace mineral(s) (<5%)
Ka-4	Calcite, Glauconite, Fluorapatite	Dolomite, Ankerite	Orthoclase
Ka-15	Glauconite, Calcite, Fluorapatite	Dolomite, Quartz	Siderite
Ka-23	Glauconite, Calcite, Fluorapatite	Hematite, Gypsum, Quartz	----------
Ka-24	Glauconite, Calcite, Fluorapatite	Dolomite	Siderite
Ka-35	Glauconite, Calcite, Fluorapatite	Dolomite, Quartz, Ankerite	----------

4.3 Composition of phosphatic layers

Major and trace elements data for 41 phosphate, carbonate, and pelagic limestone samples are listed in appendixes 3 and 6. Minimum, maximum and average concentrations of main elements (wt.%) and trace elements (ppm) in samples taken from the base of Pabdeh formation, Kangan anticline are listed in appendixes 4. The whole-rock compositional results are divided into elements related to continental input followed by the elements (U and the REE).

Appendix 3. Phosphate layers chemical analysis results taken from the base of Pabdeh Formation, Kangan anticline

Concentration	Wt%									ppm												ppm		
	Al_2O_3	Fe_2O_3	P_2O_5	K_2O	TiO_2	Na_2O	MgO	MnO	Ca	Cu	Zn	V	Ni	Ba	Sr	Cr	Zr	Yb	Nb	Y	Ga	Hf	U	Th
Samples																								
Phosphates																								
Ka-3	4.76	8.24	9.51	3.11	0.11	0.94	3.03	0.012	>20.0	12.2	52.5	210	31.0	216	787	638	24.4	18.88	27.6	422	1.15	0.28	4.36	0.80
Ka-4	1.83	2.21	1.27	0.81	0.07	0.52	2.38	0.014	>20.0	5.29	20.9	32.7	10.0	267	867	55.2	21.3	<5.00	7.26	63.2	9.47	1.54	34.8	7.77
Ka-5	1.27	1.06	0.41	0.42	0.05	0.24	1.00	0.013	>20.0	14.5	10.5	18.2	<10.0	520	1016	11.6	17.0	<5.00	<5.00	29.5	2.45	0.27	4.51	2.11
Ka-12	1.57	1.75	0.46	0.62	0.07	0.08	0.54	0.010	>20.0	5.00	173	28.7	15.9	12.4	707	43.9	24.7	<5.00	<5.00	15.8	3.82	0.57	11.2	1.35
Ka-13	1.75	2.51	3.89	0.85	0.05	0.23	0.84	0.009	>20.0	24.1	70.8	107	23.4	12.2	790	82.5	16.3	<5.00	13.0	64.1	1.30	0.40	4.34	0.85
Ka-14	4.50	8.18	11.11	2.77	0.12	0.31	1.72	0.013	>20.0	25.0	53.5	182	27.0	987	871	597	23.7	20.7	23.8	466	2.24	0.40	22.8	1.11
Ka-15	4.18	8.80	7.15	2.48	0.12	0.19	1.62	0.015	19.3	7.38	55.1	139	38.0	194	667	491	29.4	17.2	18.5	381	7.12	1.52	40.5	7.13
Ka-16	2.52	18.97	3.58	1.27	0.09	0.09	0.98	0.025	16.7	<5.00	29.6	62.9	74.4	52.8	469	183	58.0	10.1	7.56	192	7.65	1.15	19.9	7.39
Ka-17	2.30	4.01	2.48	1.06	0.08	0.10	1.20	0.016	>20.0	<5.00	20.5	46.8	14.7	573	579	139	25.1	6.85	6.44	138	4.11	0.31	8.80	3.96
Ka-21	1.77	2.35	2.16	0.81	0.06	0.06	0.62	0.010	>20.0	51.9	136	126	18.4	14.4	629	77.0	18.1	<5.00	15.4	53.8	2.50	0.42	9.01	0.53
Ka-23	4.62	8.07	9.38	2.75	0.12	0.21	1.66	0.014	18.4	115	80.8	176	26.9	167.5	656	567	28.2	15.7	22.4	365	1.97	0.20	12.6	1.09
Ka-24	4.27	6.85	6.99	2.32	0.12	0.20	1.52	0.014	19.7	154	58.1	143	39.4	199	682	463	15.1	15.4	18.5	342	7.50	1.45	39.8	5.50
Ka-25	3.83	5.47	4.79	1.91	0.12	0.16	1.30	0.014	>20.0	16.1	40.9	105	25.9	20.6	574	324	10.0	11.6	14.6	255	7.29	0.98	25.3	6.40
Ka-26	4.84	7.90	7.77	2.34	0.14	0.22	1.87	0.014	19.0	101	51.7	164	36.1	58.2	632	564	20.3	17.7	22.9	392	6.10	0.34	17.0	5.27
Ka-27	2.16	1.82	0.34	0.50	0.10	0.06	0.50	0.016	>20.0	65.1	24.0	33.3	13.6	191	880	23.1	28.4	1.86	<5.00	22.9	8.75	1.66	28.4	7.52
Ka-32	1.63	2.24	0.98	0.74	0.05	0.11	0.86	0.009	>20.0	6.14	<10.0	35.5	18.5	8.88	476	54.4	23.1	<5.00	5.25	20.7	4.52	0.74	7.26	0.72
Ka-33	0.83	0.95	0.53	0.32	0.04	0.02	0.37	0.009	>20.0	10.5	10.2	54.4	<10.0	8.74	472	26.3	13.4	<5.00	7.14	16.6	1.60	0.35	7.26	0.87
Ka-34	4.10	8.18	7.53	2.39	0.12	0.20	1.77	0.013	19.9	13.6	43.3	154	23.8	164	720	513	28.9	15.9	21.4	350	0.73	0.32	3.99	0.59
Ka-35	4.94	7.26	6.99	2.50	0.15	0.20	1.73	0.012	18.9	92.3	50.4	149	31.4	60.7	687	523	37.9	15.6	19.9	346	6.59	1.15	22.7	5.78
Ka-36	2.59	2.91	1.53	0.91	0.10	0.09	0.77	0.018	>20.0	281	29.3	53.2	15.5	20.4	563	84.8	29.9	<5.00	8.12	84.0	8.11	1.73	26.6	7.00
Ka-37	4.48	6.15	5.60	2.16	0.14	0.20	1.69	0.018	>20.0	373	53.4	119	28.4	129	603	401	20.1	13.2	15.9	292	3.69	0.26	4.61	2.83
Ka-38	3.06	3.84	2.57	1.28	0.12	0.14	1.43	0.018	>20.0	383	39.9	75.7	17.4	51.9	567	166	27.5	7.07	11.5	140	7.52	0.74	21.6	6.17
Ka-39	1.75	1.90	0.81	0.58	0.07	0.07	0.75	0.019	>20.0	245	24.0	37.0	<10.0	226	542	30.6	24.8	<5.00	5.87	43.8	5.05	0.73	9.48	4.09
Ka-40	2.05	2.73	0.95	0.62	0.09	0.09	0.15	0.018	>20.0	168	27.6	20.5	22.8	24.8	513	21.8	34.2	<5.00	<5.00	61.4	2.25	0.39	1.71	1.98
Limestone																								
Ka-2	1.32	1.29	0.24	0.56	0.06	0.36	0.86	0.009	>20.0	5.65	92.8	31.0	14.9	15.7	692	26.0	20.7	<5.00	5.36	14.4	12.2	0.44	0.37	0.75
Ka-8	5.63	2.42	0.55	0.96	0.26	0.12	0.72	0.007	>20.0	36.3	54.8	75.9	38.2	33.9	835	94.0	70.0	<5.00	12.2	31.5	1.68	0.43	0.19	1.29
Ka-10	4.49	1.81	0.19	0.78	0.21	0.11	0.58	0.007	>20.0	59.1	50.6	56.5	27.6	40.7	834	48.7	52.9	<5.00	8.35	14.0	5.81	1.44	0.42	3.21
Ka-11	2.90	4.98	2.06	1.65	0.08	0.10	1.05	0.011	>20.0	52.3	32.5	67.0	22.3	68.6	635	187	30.9	<5.00	9.45	48.9	4.90	1.15	0.43	2.44
Ka-28	5.50	2.49	0.85	0.96	0.26	0.09	0.70	0.007	>20.0	25.0	116	74.5	33.8	40.9	809	86.1	70.1	<5.00	12.2	36.8	2.17	0.62	0.25	1.65
Ka-31	3.04	6.30	0.78	2.02	0.07	0.17	1.28	0.011	>20.0	5.43	35.3	65.7	27.1	35.7	507	221	37.9	<5.00	8.85	19.8	2.52	0.81	0.25	2.10
Ka-41	7.88	2.85	1.08	1.51	0.36	0.15	1.01	0.013	>20.0	10.0	17.0	87.1	19.9	86.0	523	79.5	98.5	<5.00	14.8	56.5	2.45	0.29	0.28	2.19
Pelagic limestone																								
Ka-1	1.17	1.23	0.27	0.52	0.05	0.37	0.51	0.009	>20.0	10.1	81.3	24.0	13.7	17.0	720	23.1	17.5	<5.00	<5.00	13.8	9.27	0.25	5.10	3.93
Ka-9	5.27	2.95	0.84	1.05	0.24	0.15	0.79	0.009	>20.0	52.3	73.5	74.6	35.2	35.4	809	93.4	68.1	<5.00	11.8	44.5	6.24	1.51	5.76	3.25
Ka-19	1.94	4.03	1.34	1.19	0.05	0.05	0.76	0.010	>20.0	13.3	76.5	51.9	15.4	8.17	546	134	24.6	<5.00	7.20	23.9	5.01	1.29	3.70	2.54
Ka-29	2.19	2.31	2.40	0.71	0.08	0.13	0.72	0.009	>20.0	7.53	133	59.3	17.0	25.4	694	77.5	17.6	<5.00	8.14	72.5	5.55	1.39	6.95	3.09

Appendix 4: Minimum, maximum and average concentrations of main elements (wt.%) and trace elements (ppm) in samples taken from the base of Pabdeh formation, Kangan anticline

Element	Min	Max	Mean (All samples)	Mean (Phosphate)	Mean (Limestone)	Mean (Pelagic limestone)
Al_2O_3	0.83	7.88	3.23	2.98	4.39	2.64
Fe_2O_3	0.95	18.97	4.49	5.18	3.16	2.63
P_2O_5	0.19	11.11	3.13	4.12	0.82	1.21
K_2O	0.32	3.11	1.36	1.48	1.21	0.87
TiO_2	0.04	0.36	0.11	0.10	0.19	0.11
Na_2O	0.02	0.94	0.19	0.20	0.16	0.18
MgO	0.15	0.03	1.12	1.26	0.89	0.70
MnO	0.007	0.025	0.01	0.01	0.01	0.01
Cu	5.00	383.00	74.12	98.60	27.68	20.81
Zn	10.20	173.00	56.45	50.26	57.00	91.08
V	18.20	210.00	84.01	94.70	65.39	52.45
Ni	10.00	74.40	25.55	26.31	26.26	20.33
Ba	8.17	987.00	131.06	174.15	45.93	21.49
Sr	469.00	1016.00	672.94	664.54	690.71	692.25
Cr	11.60	638.00	204.30	253.34	106.04	82.00
Zr	10.00	98.50	31.67	24.99	54.43	31.95
Nb	5.25	27.60	13.05	14.65	10.17	9.05
Y	13.80	466.00	140.95	189.87	31.70	38.68
Ga	0.73	12.20	4.89	4.73	4.53	6.52
Hf	0.20	1.73	0.79	0.75	0.74	1.11
U	0.19	39.80	11.78	16.19	0.31	5.38
Th	0.53	7.77	3.29	3.70	1.95	3.20

Appendix5. Elements correlation table showing the correlation coefficients (R^2).

	Al	Ba	Cr	Cu	Fe	K	Mg	Mn	Na	Ni	P	Sr	Ti	Ba	V	Zn	Nb	Y	Zr	Ga	Hf	Th	U
Al	1																						
Ba	0.298	1																					
Cr	0.803**	0.297	1																				
Cu	0.282	0.002	0.115	1																			
Fe	0.785**	0.31	0.886**	0.056	1																		
K	0.830**	0.332	0.982**	0.154	0.905**	1																	
Mg	0.608**	0.539**	0.802**	0.062	0.709**	0.802**	1																
Mn	0.057	0.331	0.014	0.396	0.285	0.055	0.096	1															
Na	0.371	0.502*	0.599**	0.039	0.492*	0.609**	0.849**	-0.059	1														
Ni	0.757**	0.062	0.764**	0.052	0.815**	0.782**	0.508**	0.028	0.376	1													
P	0.682**	0.302	0.958**	0.168	0.898**	0.950**	0.808**	0.045	0.676**	0.734**	1												
Sr	0.215	0.469*	0.105	-0.119	-0.072	0.139	0.274	-0.365	0.470*	0	0.072	1											
Ti	0.920**	0.277	0.645**	0.341	0.566**	0.688**	0.485*	0.167	0.207	0.669**	0.522**	0.187	1										
Ba	0.298	1.000**	0.297	0.002	0.31	0.332	0.539**	0.331	0.502*	0.062	0.302	0.469*	0.277	1									
V	0.759**	0.168	0.917**	0.209	0.761**	0.890**	0.629**	-0.178	0.469*	0.726**	0.898**	0.142	0.595**	0.168	1								
Zn	0.468*	-0.11	0.455*	0.141	0.316	0.476*	0.119	-0.286	0.143	0.547**	0.411*	0.332	0.408*	-0.11	0.568**	1							
Nb	0.797**	0.217	0.931**	0.214	0.758**	0.915**	0.722**	-0.16	0.563**	0.715**	0.907**	0.2	0.644**	0.217	0.978**	0.557**	1						
Y	0.735**	0.445*	0.932**	0.219	0.920**	0.943**	0.839**	0.219	0.678**	0.716**	0.965**	0.107	0.606**	0.445*	0.832**	0.314	0.861**	1					
Zr	0.323	0.082	0.058	-0.02	0.268	0.138	-0.068	0.307	-0.299	0.179	-0.062	-0.075	0.362	0.082	-0.044	0.025	-0.051	0.05	1				
Ga	0.023	0.079	-0.106	0.079	-0.018	-0.108	-0.005	0.582**	-0.169	0.002	-0.204	-0.163	0.129	0.079	-0.303	-0.252	-0.255	-0.078	0.184	1			
Hf	-0.124	-0.11	-0.118	0.018	-0.013	-0.107	-0.116	0.328	-0.215	-0.009	-0.152	-0.102	-0.022	-0.11	-0.214	-0.154	-0.195	-0.092	0.17	0.798**	1		
Th	0.17	0.266	-0.037	0.074	0.082	-0.015	0.078	0.662**	-0.06	0.072	-0.124	-0.025	0.276	0.266	-0.236	-0.232	-0.17	0.063	0.288	0.892**	0.661**	1	
U	0.218	0.23	0.232	0.065	0.199	0.218	0.173	0.359	0.028	0.179	0.152	0.053	0.268	0.23	0.097	0.057	0.132	0.237	0.057	0.792**	0.766**	0.746**	1

*Correlation is significant at the 0.05 level.
**Correlation is significant at the 0.01 level.

4.3.1 Elements related to detrital input

The concentrations of major elements (and some trace elements) are proxies for detrital (continental) input into phosphatic layers. Detrital clay minerals generally include Al_2O_3, Fe_2O_3, TiO_2, K_2O, Cr, and Th; these elements are relatively enriched in continental detritus compared with chemical sedimentary rocks. In particular, Al_2O_3 is a useful proxy for clay content (Abed et al., 2016). Phosphate samples have concentrations of Al_2O_3 that vary from ~0.83 to 4.9 wt.%, with an average of ~3.7 wt.% (appendix 3). A positive correlation between Al and Fe, Ti, and K (appendix 5 and Fig. 8) in the phosphate samples suggests that enrichment of these in the phosphate layers are related to a higher fraction of clay detritus. Al_2O_3 concentration of limestone samples with an average of ~4.4 wt.% is vary from 1.32 to 7.88 wt.% (appendix 3). Pelagic limestone has also Al_2O_3 from ~1.2 to ~5.3 with ~2.5 average (appendix 3). There is a positive correlation between Al and Ti (appendix 5 and Fig. 9) in the limestone and pelagic limestone samples, indicating detrital clay minerals are present in these layers. Unlike the phosphate layers, a significant positive correlation between Al with Fe and K is not seen in the limestone and limestone layers of the pelagic (Fig. 9).

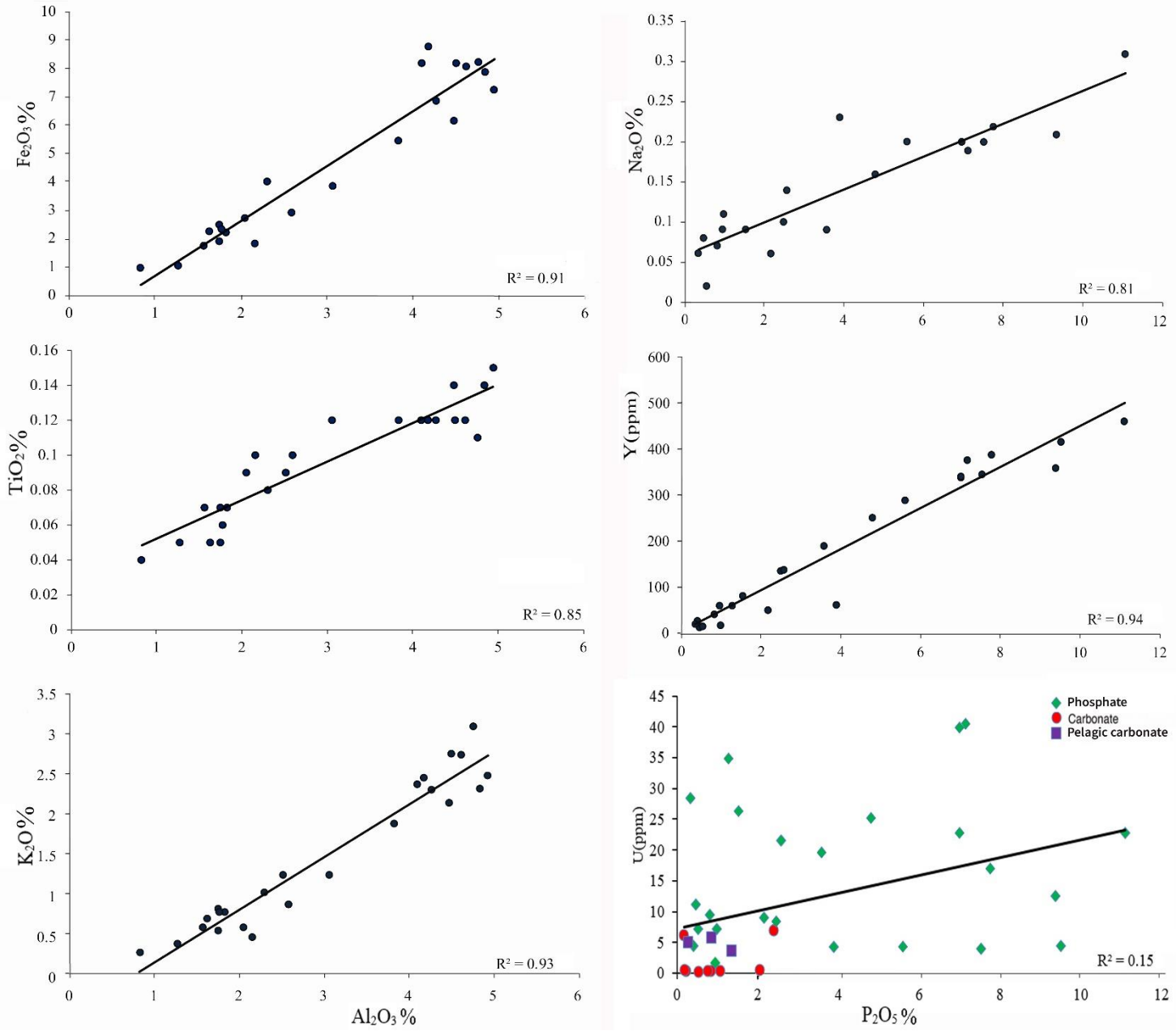

Figure 8. Binary correlation diagrams for elements with a continental origin (Al_2O_3 with Fe_2O_3, TiO_2 and K_2O) and elements accompanied by phosphorus enrichment (P_2O_5 with Na_2O, Y and U) in marine sedimentary phosphate samples of the base of Pabdeh Formation of Kangan anticline. In the U vs P_2O_5 diagram, R^2 value is for all the data.

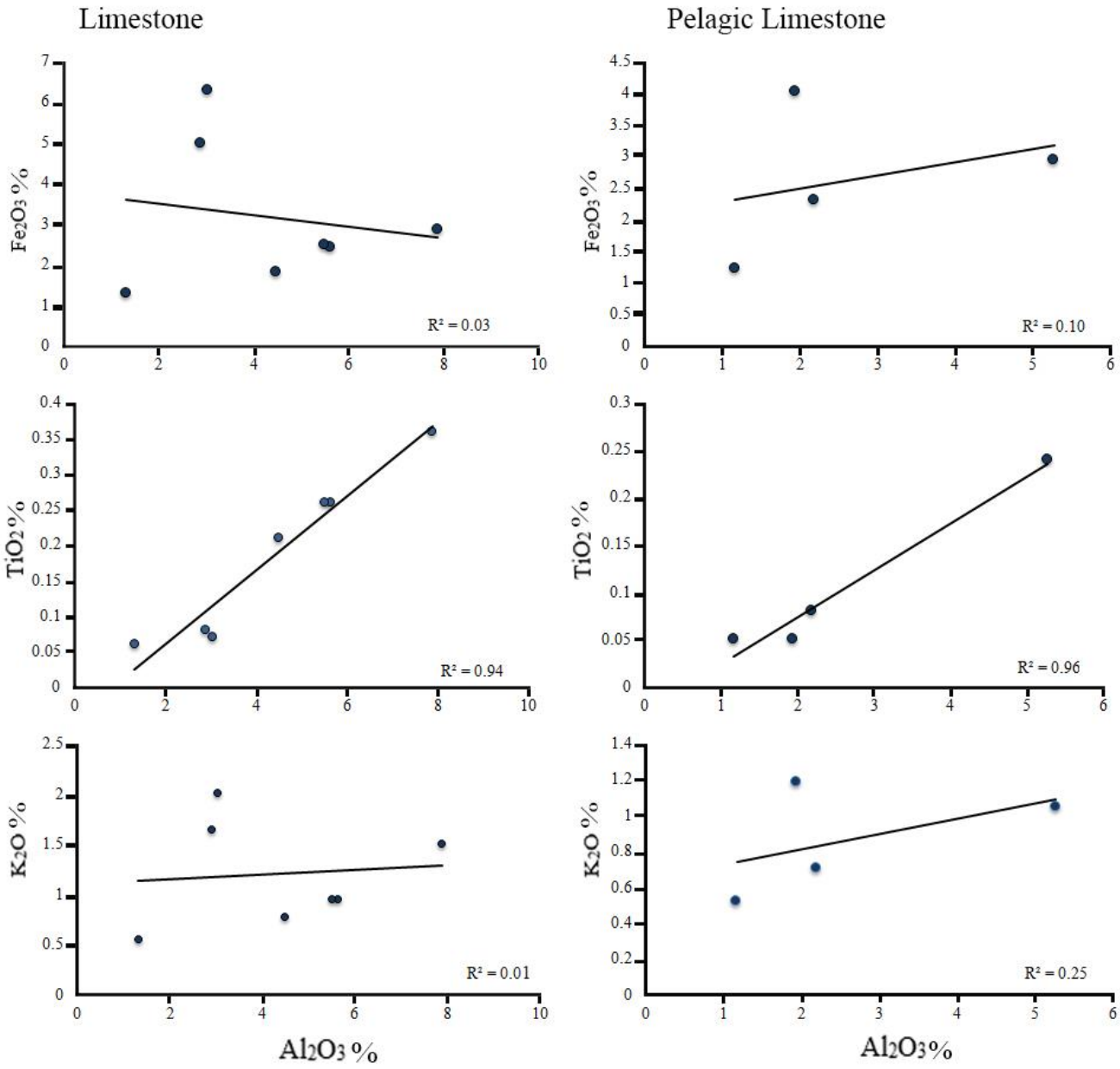

Figure 9. Binary correlation diagrams for elements with a continental origin (Al_2O_3 with Fe_2O_3, TiO_2 and K_2O) in limestone and pelagic limestone samples of the base of Pabdeh Formation of Kangan anticline.

4.3.2 REE, U and Th Concentrations

The total concentration of REE (ΣREE) in all phosphate samples vary from ~32 to 792 ppm (appendix 6 and appendix 7); phosphatic horizons is ~392 ppm. In phosphatic horizons of Khormuj anticline, the average ΣREE value is 405.8 ppm (Haddad et al., 2023).

Appendix6. ICP-MS analysis results of the phosphate, limestone and pelagic limestone layers taken from the base of Pabdeh Formation, Kangan anticline (ppm)

Samples	La	Ce	Pr	Nd	Sm	Eu	Gd	Tb	Dy	Ho	Er	Tm	Yb	Lu	Y	ΣREE	ΣLREE	ΣHREE	ΣLREE/ ΣHREE	Ce/Ce*	Y/Y*	Eu/Eu*	La/Yb	EF
Phosphate																								
Ka-3	9.87	5.57	1.69	8.33	1.20	0.32	1.25	0.21	1.32	0.32	0.94	0.20	bdl	0.19	422	31.42	26.99	4.43	6.09	0.31	51.20	1.25	-	0.17
Ka-4	206	149	47.4	181.2	41.7	9.83	38.3	6.73	39.8	8.95	25.7	3.86	18.8	3.05	63.2	780.12	634.80	145.33	4.37	0.35	0.27	1.16	10.90	4.22
Ka-5	34.7	24.5	7.36	29.3	6.27	1.71	7.19	1.14	6.97	1.68	4.45	0.77	bdl	0.67	29.5	126.63	103.78	22.86	4.54	0.35	0.69	1.20	-	0.69
Ka-12	23.4	17.2	4.74	21.7	4.29	0.97	4.33	0.71	4.23	1.02	2.82	0.40	bdl	0.38	15.8	86.11	72.22	13.89	5.20	0.38	0.61	1.06	-	0.47
Ka-13	9.17	6.99	1.37	8.55	1.13	0.26	1.15	0.19	1.15	0.28	0.89	0.11	bdl	0.13	64.1	31.37	27.47	3.90	7.04	0.45	9.02	1.09	-	0.17
Ka-14	30.8	27.0	6.63	27.7	5.89	1.52	6.41	0.90	5.63	1.37	3.85	0.55	bdl	0.51	466	118.76	99.54	19.22	5.18	0.44	13.36	1.16	-	0.64
Ka-15	220	138	48.0	190	41.2	9.3	38.0	6.46	39.1	9.39	25.5	3.68	20.7	3.09	381	791.92	645.98	145.94	4.43	0.31	1.58	1.10	10.62	4.29
Ka-16	181	116	42.9	162	38.0	10.1	35.5	6.14	31.4	8.67	25.0	3.58	17.2	2.95	192	680.21	549.73	130.47	4.21	0.30	0.92	1.29	10.56	3.68
Ka-17	88.1	56.1	21.4	86.2	18.7	4.51	18.5	2.89	18.9	4.44	11.9	1.85	10.1	1.53	138	345.11	275.02	70.09	3.92	0.30	1.20	1.14	8.73	1.87
Ka-21	11.1	9.53	2.09	12.4	1.67	0.33	1.52	0.30	1.61	0.41	1.27	0.18	bdl	0.17	53.8	42.64	37.19	5.45	6.82	0.46	5.26	0.97	-	0.23
Ka-23	25.7	25.7	5.32	24.4	4.61	1.13	4.95	0.79	4.95	1.15	3.28	0.45	bdl	0.44	365	102.82	86.81	16.01	5.42	0.51	12.16	1.11	-	0.56
Ka-24	168	124	38.3	150	32.0	7.81	30.4	5.62	30.5	7.39	18.2	2.70	15.7	2.33	342	633.86	521.11	112.75	4.62	0.36	1.81	1.18	10.72	3.43
Ka-25	164	113	37.4	146	30.5	8.58	30.7	5.40	31.0	7.67	20.0	2.87	15.4	2.62	255	614.47	498.74	115.73	4.31	0.33	1.32	1.32	10.65	3.33
Ka-26	124	84.3	28.4	109	24.6	5.53	19.5	3.78	21.8	5.40	15.1	2.17	11.6	1.90	392	457.51	376.11	81.40	4.62	0.33	2.87	1.19	10.68	2.48
Ka-27	191	131	45.4	165	38.2	8.58	28.3	5.89	35.7	8.54	21.8	3.47	17.7	2.94	22.9	703.20	578.91	124.29	4.66	0.32	0.10	1.23	10.84	3.81
Ka-32	9.26	10.2	2.19	10.3	1.84	0.45	1.70	0.31	1.77	0.47	1.24	0.20	bdl	0.17	20.7	40.17	34.31	5.86	5.86	0.52	1.80	1.20	-	0.22
Ka-33	10.4	9.29	2.41	12.0	2.19	0.52	1.93	0.37	2.02	0.51	1.38	0.22	bdl	0.20	16.6	43.45	36.80	6.64	5.54	0.43	1.30	1.18	-	0.24
Ka-34	10.2	7.17	1.97	9.14	1.45	0.32	1.26	0.26	1.35	0.38	1.22	0.21	bdl	0.23	350	35.16	30.25	4.91	6.16	0.37	38.57	1.11	-	0.19
Ka-35	171	115	35.5	151	31.8	6.93	24.7	5.18	26.9	6.98	20.2	2.81	15.9	2.35	346	616.31	511.37	104.94	4.87	0.34	2.00	1.16	10.75	3.34
Ka-36	171	115	38.6	149	34.8	7.81	28.8	5.66	31.0	8.07	20.1	3.27	15.6	2.67	84.0	631.39	516.27	115.12	4.48	0.33	0.42	1.16	10.99	3.42
Ka-37	43.5	30.7	10.7	37.1	8.67	2.03	9.12	1.50	8.89	2.30	5.82	0.92	bdl	0.84	292	162.09	132.68	29.41	4.51	0.33	5.12	1.07		0.88
Ka-38	143	97.9	35.8	125	30.6	6.92	28.7	5.35	29.5	7.22	19.3	2.90	13.2	2.41	140	548.41	439.91	108.50	4.05	0.32	0.76	1.10	10.90	2.97
Ka-39	70.9	50.0	17.9	63.8	15.4	3.43	15.4	2.67	15.3	3.83	10.0	1.53	7.07	1.39	43.8	278.60	221.36	57.24	3.87	0.32	0.45	1.05	10.02	1.51
Ka-40	24.5	15.9	5.16	19.5	4.29	0.86	4.13	0.74	4.35	1.13	2.99	0.50	bdl	0.50	61.4	84.49	70.17	14.33	4.90	0.33	2.20	0.96	-	0.46
PAAS	38.2	79.6	8.83	33.9	5.55	1.08	4.66	0.77	4.68	0.99	2.85	0.40	2.82	0.43	27	183.00	164.50	16.97	9.69	9.69	1.02	0.66		
Limestone																								
Ka-2	9.49	5.05	1.30	9.21	0.89	0.22	0.82	0.15	0.79	0.19	0.63	0.10	bdl	0.15	14.4	29.01	26.16	2.84	9.21	0.33	2.92	1.23	-	0.16
Ka-8	17.8	10.6	3.82	15.6	3.22	0.91	2.83	0.52	3.45	0.83	2.18	0.40	bdl	0.41	31.5	62.57	51.95	10.62	4.89	0.30	1.49	1.42	-	0.34
Ka-10	26.2	25.2	5.31	24.1	4.52	1.07	4.52	0.77	4.44	0.97	2.98	0.38	bdl	0.37	14.0	100.82	86.39	14.44	5.98	0.49	0.54	1.11	-	0.55
Ka-11	11.0	13.6	2.12	10.4	1.56	0.34	1.43	0.23	1.38	0.31	0.84	0.15	bdl	0.15	48.9	43.57	39.07	4.50	8.69	0.65	5.91	1.08	-	0.24
Ka-18	69.86	43.64	15.63	60.71	14.46	3.62	14.94	2.37	14.34	3.58	9.84	1.42	6.85	1.24	10.9	262.51	207.92	54.59	3.81	0.30	0.12	1.16	10.20	1.42
Ka-28	14.5	8.04	2.87	14.4	2.27	0.43	1.74	0.38	2.03	0.52	1.63	0.27	bdl	0.25	36.8	51.21	42.53	8.68	4.90	0.29	2.84	1.01	7.82	0.28
Ka-31	34.7	30.2	8.37	31.1	7.85	1.60	6.40	1.24	6.68	1.66	4.75	0.70	bdl	0.60	19.8	135.93	113.91	22.02	5.17	0.41	0.47	1.06	-	0.74
Ka-41	33.6	20.8	7.25	30.3	5.87	1.37	6.15	1.13	6.38	1.65	4.70	0.73	bdl	0.68	56.5	120.66	99.25	21.42	4.63	0.31	1.38	1.07	-	0.65
Pelagic limestone																								
Ka-1	34.5	37.6	7.75	30.4	6.54	1.39	5.40	0.92	5.43	1.32	3.22	0.57	bdl	0.44	13.8	135.55	118.25	17.30	6.84	0.53	0.41	1.10	-	0.73
Ka-9	20.1	21.2	4.24	18.1	3.34	0.81	3.66	0.55	3.38	0.73	2.16	0.34	bdl	0.29	44.5	78.79	67.69	11.10	6.10	0.53	2.26	1.09	-	0.43
Ka-19	9.93	13.8	1.98	8.96	1.52	0.34	1.27	0.21	1.29	0.30	0.79	0.13	bdl	0.13	23.9	40.61	36.49	4.13	8.84	0.72	3.07	1.14	-	0.22
Ka-29	22.1	23.4	4.61	21.0	3.86	0.82	3.06	0.55	3.52	0.84	2.17	0.36	bdl	0.32	72.5	86.55	75.73	10.82	7.00	0.53	3.35	1.12	-	0.47
Sea water	20.8	9.64		21.1	4.32	0.823	5.2		5.61		4.94													

bdl: below detection limit

Appendix 7. Minimum, maximum and average concentrations of rare earth elements (ppm) in samples taken from the base of Pabdeh formation, Kangan anticline

	Phosphate			Carbonate			Pelagic carbonate		
Element	Min	Max	Mean	Min	Max	Mean	Min	Max	Mean
La	9.17	219.66	89.21	9.49	69.86	27.16	9.93	34.49	21.65
Ce	5.57	148.86	61.62	5.05	43.64	19.65	13.76	37.64	23.99
Pr	1.37	47.97	20.35	1.30	15.63	5.83	1.98	7.75	4.64
Nd	8.33	189.59	79.10	9.21	60.71	24.48	8.96	30.43	19.61
Sm	1.13	41.75	17.54	0.89	14.46	5.08	1.52	6.54	3.82
Eu	0.26	10.09	4.15	0.22	3.62	1.20	0.34	1.39	0.84
Gd	1.15	38.32	15.19	0.82	14.94	4.85	1.27	5.40	3.35
Tb	0.19	6.73	2.88	0.15	2.37	0.85	0.21	0.92	0.56
Dy	1.15	39.80	16.47	0.79	14.34	4.94	1.29	5.43	3.40
Ho	0.28	9.39	4.07	0.19	3.58	1.22	0.30	1.32	0.80
Er	0.89	25.73	10.95	0.63	9.84	3.44	0.79	3.22	2.08
Tm	0.11	3.86	1.64	0.10	1.42	0.52	0.13	0.57	0.35
Yb	70.7	20.68	14.91	1.86	6.85	4.35	-	-	-
Lu	0.13	3.09	1.40	0.15	1.24	0.48	0.13	0.44	0.29
ΣREE	31.37	791.92	332.76	29.01	262.51	100.78	40.61	135.55	85.37
ΣLREE	26.99	645.98	271.98	26.16	207.92	83.40	36.49	118.25	74.54
ΣHREE	3.90	145.94	60.78	2.84	54.59	17.39	4.13	17.30	10.84
ΣLREE/ΣHREE	3.87	7.04	4.99	3.81	9.21	5.91	6.10	8.84	7.19

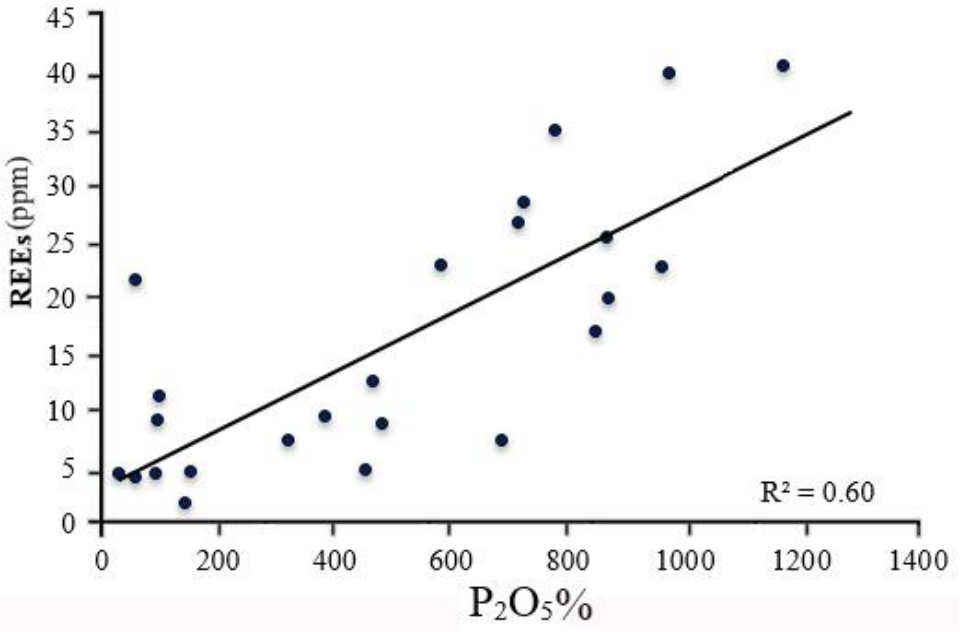

Figure 11. Variations of the total concentration of the Rare Earth Elements (ΣREE) vs. P_2O_5% in marine sedimentary phosphate samples of Kangan anticline's Pabdeh Formation

ΣREE is also positively correlated with increases in P_2O_5 (r=0.60) (Fig. 11). Enrichment factors (EF) of the REE ($\Sigma REE_{(sample)}$/ $\Sigma REE_{(PAAS)}$) at the base of the Paleocene Pabdeh Formation vary between 0.28 and 5.54 (EF of Khormuj anticline phosphatic horizons, 0.26 to3.71, Haddad et al., 2023). REE concentrations of phosphate samples normalized to the average post-Archean Australian Sedimentary Shale (PAAS) (McLennan, 1989) show similar patterns to those of seawater, such as negative Ce anomalies, slight positive Eu anomalies and positive Y anomalies (Fig. 12) that is similar to the Khormuj anticline phosphatic samples Haddad et al., 2023.

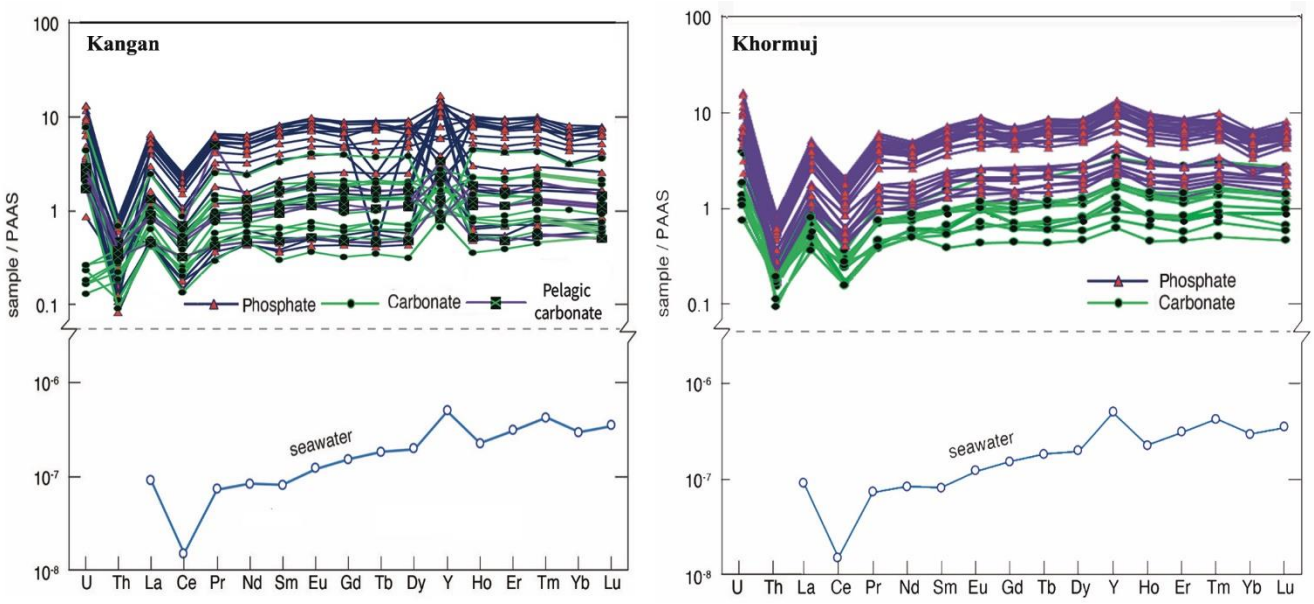

Figure 12. Post-Archean average Australian shale (PAAS)-normalized Rare earth element patterns of samples from the Kangan (this study) and Khormuj (Haddad et al., 2023) anticlines. Also plotted are the PAAS-normalized values of modern Central Atlantic seawater from Høgdahl et al. (1968). PAAS values from Taylor and McLennan (1985). Note that some values of Yb were below the detection limit an no symbols are plotted at Yb for these samples.

PAAS-normalized REE patterns of phosphate samples are nearly flat with a gentle and positive slope from the LREE to the HREE (Fig. 12) like as Khormuj phosphatic samples. Therefore, there is slight enrichment of HREE over the LREE in the phosphate layers compared with PAAS. Fractionation of LREE from the HREE can be quantified by the ratio $(\Sigma LREE/\Sigma HREE)_N$ (e.g. Mercadier et al., 2011). Phosphate layers in the Kangan anticline have $(\Sigma LREE/\Sigma HREE)_N$ ratios ranging from 0.40 to 0.74 (appendixes 6 and 7) (Khormuj anticline phosphatic horizons $(\Sigma LREE/\Sigma HREE)_N$ ratios, 3.5 to 5.1, Haddad et al., 2023) indicating fractionation of the HREE relative to the LREE when compared with PAAS.

In the phosphate samples, concentrations of U vary from 1.7 to 40.5 ppm (appendix 3) (U concentrations of phosphatic Khormuj samples 1.59 to 55.6 ppm, Haddad et al., 2023). Phosphate

samples of the Kangan anticline show U enrichment (5.22) compared to PAAS values (3.10 ppm) (McLennan, 1989) (U enrichment of phosphatic Khormuj samples 8.23, Haddad et al., 2023). Most of phosphates are enriched in uranium relative to the PAAS (Fig. 10a). Carbonate samples do not display uranium enrichment relative to PAAS (Fig. 10a). Pelagic limestone samples are slightly enriched in U relative to carbonates and to the PAAS (Fig. 10a). Comparison of PAAS-Normalized values of U in studied samples from the base of the Pabdeh Formation of Kangan anticline and Khormuj anticline is illustrated in fig. 10b. Dissimilar to the Khormuj samples, the investigated samples do not show a robust positive correlation between concentrations of U and P_2O_5 (Fig.8 and appendix 4). Like as Khormuj phosphatic layers, Phosphatic layers of the Kangan anticline do not show enrichment of Th compared to PAAS and neither do limestone or pelagic limestone samples (Fig. 10a).

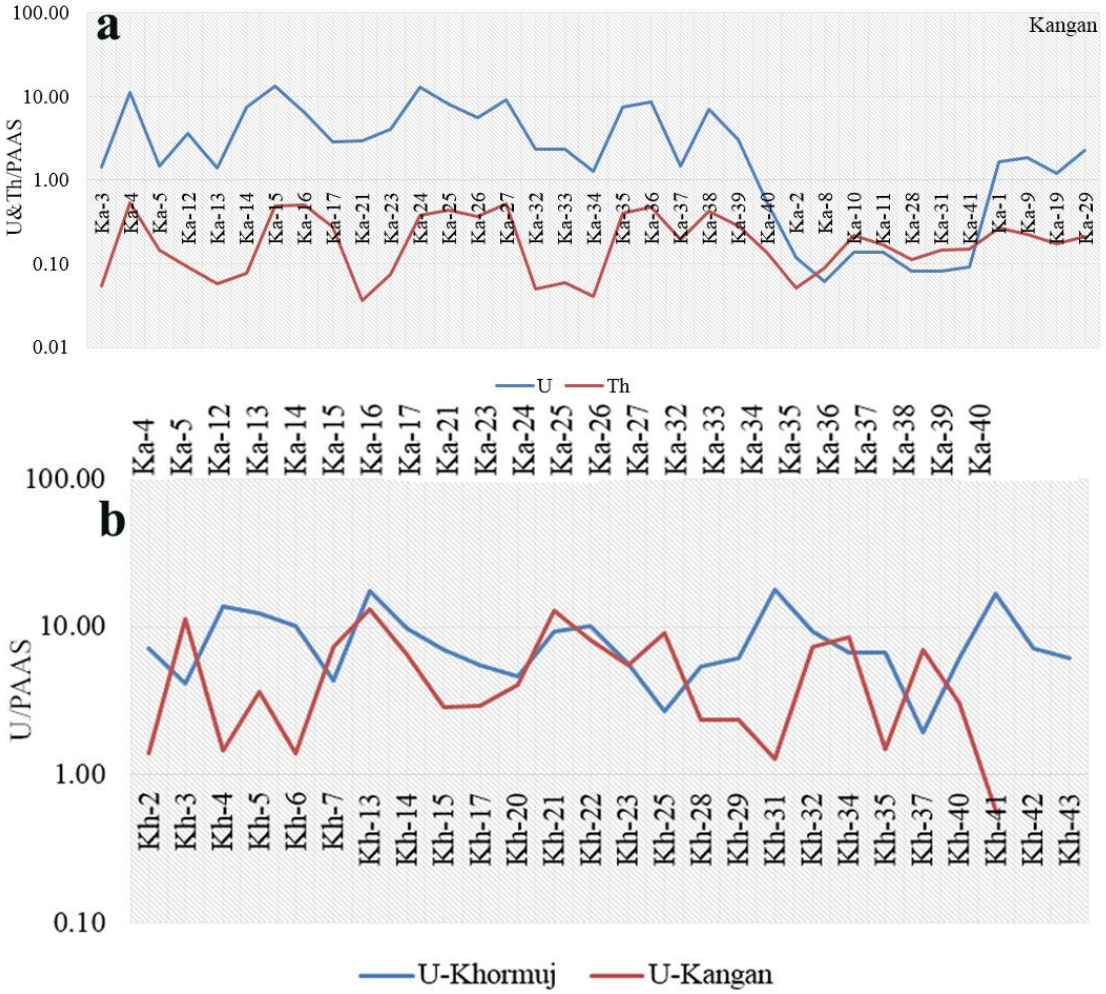

Figure 10. a: PAAS-normalized values for U and Th of samples of Pabdeh Formation of Kangan anticline. Note the relative depletion of U in the carbonate and Pelagic carbonate samples compared with the phosphate samples. b: Comparison of PAAS-Normalized values of U in studied samples from the base of the Pabdeh Formation of Kangan anticline and Khormuj anticline.

5. Discussion

5.1 Paleodepositional environment

There are many factors that can influence the deposition of phosphate deposits. These factors include depth of deposition (Khoshnoodi and Ziapour 2022; Dahlkamp 2009, Avilés et al., 2006), oxidation and reduction conditions (Eh) and the pH of water, phosphate mineral assemblages, the abundance of organic matter, phosphate grade, and paleoclimatic conditions (Baturin and

Kochenov 2001, Dahlkamp 2013) as well as weathering (Abed 2013). Furthermore, these factors also influence REE and U substitution into francolite (Simandl et al. 2011, Voyseh, 2017), which is the dominant mineral host for these metals in phosphate deposits (Zhang et al. 2021). Hence, the depositional environment will influence the prospectivity of phosphate deposits for metals of economic interest. Our analyses of phosphatic layers—as well as bounding pelagic limestone and limestone layers—in the Pabdeh Formation of Kangan anticline can be used to infer depositional conditions and to evaluate the mechanisms responsible for the enrichment of HREE and U in these rocks.

The pelagic limestone layers beneath the lower limestone layers have mudstone textures with microfractures, bioclasts, and insignificant pelagic foraminifera, organic matter with laminations and no glauconite (Fig. 5o). These textures are compatible with a low-energy and very deep depositional environment. The pelagic limestone layers are covered by limestone across a sharp but non-erosional boundary (Fig. 3 and Fig. 4).

Beneath and above the phosphatic layers are the limestone layers with wackstone to packstone textures and abundant plankton foraminiferal shells in a micritic matrix (Fig. 5m-n). A small number of green glauconite grains are present in limestone layers (Fig. 5m) in the Pabdeh Formation of Kangan anticline. These textures are interpreted to represent an offshore depositional basin connected to the open ocean (e.g. Flugel, 2004; Flugel and Munnecke, 2010). In the lower limestone layers, the presence of *Morozovella, Conicotruncata Sp.* microfossils rimmed with calcite cement (Fig. 5n) suggest tropical to subtropical conditions during deposition of the Kangan anticline phosphate layers (e.g., Subbotina, 1947).

The phosphatic layers within the Kangan anticline represent a complex archive of biogenic phosphate grains (pellets, ooids, intraclasts, vertebrate bone fragments, shells, teeth, and scales of fish) (Fig. 5d–e), terrigenous inputs (such as clay minerals and quartz).

The depositional environment of the phosphate deposits can be inferred from grain textures and internal zoning of the phosphatic grains. Pellets (Fig. 5a) and phosphate intraclasts (Fig. 5c) were likely derived from autogenous phosphates; they suggest turbulence during deposition and a comparatively shallow environment (e.g., Benitez-Nelson et al., 2004). Oolites with concentric layers (now broken due to diagenesis; Fig. 5b) are interpreted to record multi-stage deposition on the seafloor, burial, and displacement (Benitez-Nelson et al., 2004). The presence of reducing conditions during deposition is suggested by yellow- to the orange-colored organic matter in phosphate layers (Fig. 5f) (e.g. Abed et al., 2016). In phosphorites, the phosphate mud (Fig. 5k) probably precipitated from phosphorus ion-enriched solutions in pores (e.g. Felitsyn and Morad, 2002; Abed et al., 2016; Haddad et al., 2023). High proportions of organic matter along with sulfide minerals such as pyrite (Fig. 5f) are observed in some samples (Fig. 6a-b-c-d and Fig. 7f) and are inferred to represent post-depositional sulfidation (e.g., Pestitschek et al., 2012). The organic matter proportion in the phosphate samples is lower than the non-phosphate samples; this is interpreted to represent the vestiges of organic matter decomposition during phosphatization (Fig. 5f) (Balthasar, 2007; Hiatt et al., 2015).

Three forms phosphatization was observed in glauconate grains: phosphatization from the margin of glauconite to the mineral center (Fig. 5g); phosphatization from the center of the glauconite to the edge of the mineral (Fig. 5h); vermiculated phosphatization, where apatite is scattered throughout the glauconite (Fig. 5i). Glauconite also occurs in foraminifera chambers (Fig. 7g-h-j-k). Green chert, which is commonly associated with upwelling environments (Abed, 2013),

phosphorite formation (Abed, 2013) and of biochemical origin (Abed et al., 2016), were observed in the thin sections (Fig. 5l and Fig. 7h).

Framboidal pyrite grains are disseminated across samples (Fig. 6a-b). Framboidal pyrite is probably a product of the bacteria and fungi (Virtasalo et al., 2010) conversion of sulfate and in-situ iron monosulfide (Fazio et al., 2007); this process was likely related to syngenetic reducing conditions (Gál et al., 2020; Liu et al., 2020). Pyrite may have been produced by sulfate-reducing bacteria in seawater (e.g., Voronin, 2019). Cubic pyrite was also observed in samples (Fig. 6c-d and Fig. 7f); these were been created due to the reduced environment. Oxidation of syngenetic pyrite is inferred to have produced diagenetic (secondary) iron oxides (hematite and goethite) (Fig. 7c-n).

The paleodepositional environment can also be reconstructed using the pelagic limestone, limestone, and phosphate samples compositions, particularly the REE pattern. Cerium anomalies exist in the samples (Fig. 12), and probably formed by Ce deposition with redox-sensitive metals (e.g., iron, manganese) under oxic seawater conditions (e.g. Tostevin et al., 2016). Nevertheless, Ce anomalies are less pronounced in the phosphate samples (Fig. 12), indicating less oxidized conditions than deposition of the pelagic limestone and limestone layers.

A paleodepositional model is presented based on the combination of the textures and composition information of the Pabdeh Formation described above. Pelagic limestone layers were deposited in the basin with higher depth than limestone layer. Moving upward from the pelagic limestone to the bottom limestone layer, the basin depth gradually decreased. Subsequently, phosphatization and accumulation of phosphate in the margin carbonate ramp environment was caused by a depth increase and extreme upwelling currents of acidic (as a result of CO_3^{2-} and PO_4^{3-} soluble ions presented as carbonic acid and phosphoric acid) (Long et al., 2011) and cold waters

enriched in phosphate ions (PO_4^{3-}); there was high biological activity, a large amount of plankton growth, and production of organic matter on the continental shelf as a result of these upwelling currents. (Mutti and Bernoulli, 2003; James et al., 2004; Trela, 2005; Brookfield et al., 2009; Collins et al., 2014; Brandano et al., 2016; Messadi et al., 2019; Sanders and Grotzinger, 2021). Due to the existence of planktonic foraminifera, green glauconite, green biochemical chert, crystalline and framboidal pyrites, dolomite, ankerite, and the existence of organic matter, an anoxic or suboxic environment with reduced Eh and slightly alkaline pH (~7.7–8) can be considered for the time of deposition of the sandy glauconite-bearing phosphatic layer in the Kangan anticline (Baioumy, 2002; Zeebe, 2012; Bolourchifard et al., 2019). Further phosphate deposition occurred during regression and was followed deposition of the limestone layer above the sandy glauconite-bearing phosphate layer.

Primaryphosphate and glauconite facies are generally spatially related (Odin and Letolle, 1980) in the studied sections, glauconite formation requires a relatively low-energy sedimentary environment (e.g. Brookfield et al., 2009). In the following, High erosion rates, divided and transportation of the phosphatic grains in inferred for the studied samples based on the low proportion to absence of micrite in phosphatic packstones and grainstones, well-rounded pellets and ooids, lack of concentric layers in composite ooids, absence of phosphatic cement, and presence of intraclasts (Tarawneh, 2005; Arning et al., 2009; Bolourchifard et al., 2019; Haddad et al., 2020; Haddad et al. 2023). The presence of pellets, ooids and glauconite in the phosphate samples suggests deposition in a shallow coastal environment with low detrital input.

Phosphate horizons of the Pabdeh Formation in the Kangan anticline appear to have been affected by syngenetic, and diagenetic, processes. The syngenetic processes in sedimentary rocks refer to the processes that occur during the deposition and formation of them (Boggs 2014; Nichols

2009; Tucker 2001). Phosphatization, glauconitization and sulfidation (i.e., pyrite growth) in samples containing organic matter and glauconite combined with the presence of laminated phosphate provide evidence of syngenetic mineralization.

Diagenetic processes in sedimentary rocks encompass a wide range of post-depositional changes that occur after the initial deposition of sediments (Boggs 2014; Nichols 2009; Worden and Burley 2003; Tucker 2001). Diagenetic processes include glauconite formation due to an increment in the concentration of K^+ ions and/or phosphatization in glauconite by increasing concentrations of PO_4^{2-} in connate fluids during diagenesis (e.g. Banerjee et al., 2012; Baldermann et al., 2015). Replacement of foraminifera chambers by glauconite, phosphate or iron oxide (Fig. 5c-k and Fig. 7g-h-l-j-k) also suggest diagenetic mobilization of components. The presence of gypsum (Fig. 6e-f and Fig. 7a-m) is also diagnostic of diagenetic formation (e.g. Pirlet et al., 2010); gypsum mineralization may be the result of the oxidation of syngenetic sulfide minerals (generating SO_4^{2-}) coupled with the dissolution of carbonate that released Ca^{2+} into solution (Doner and Lynn, 1977, Liu et al., 2018). Furthermore, the development of euhedral hematite crystals and hematitization along pyrite margins (Fig. 6e, f and Fig. 7n) could possibly be attributed to subaerial oxidative weathering as part of a diagenetic process.

5.2 Mineral hosts of trace metals

It is essential to understand the minerals that contain trace metals in phosphate deposits to assess their economic potential (Abed et al., 2016; Hein et al., 2016; Robb, 2020). These metals can be adsorbed onto various minerals such as Fe-Mn oxides, clay minerals, apatite, sulfide minerals, and organic matter, and cation substitution in apatite can also store these metals (Emsbo

et al., 2015; Hughes and Rakovan, 2015; Zhu and Jiang, 2017). Francolite in phosphate rocks can substitute various cations and accommodate a significant portion of the total REEs (Chen et al., 2010; Hughes and Rakovan, 2018).Before we can evaluate whether ion adsorption or cation substitution is the predominant concentration mechanism of trace metals in the Pabdeh Formation phosphate deposits, we must first rule out the possibility that enrichment of trace elements are caused by an increase in the clastic component of individual samples. The presumption that all of the clay minerals —other than glauconite, which may be diagenetic in origin—are clastic in origin, like as Khormuj samples (Haddad et al., 2023) the Kangan analyzed samples have an average of lesser than 5% clastic material (as a result of Al_2O_3 value in the table 3). Fe_2O_3 and K_2O, depending on the type of clay minerals, can also exist in the mineral structure (Weaver and Pollard, 1973). In addition, the elements of TiO_2, Al_2O_3, MgO, K_2O, Ba, Hf, Nb, and Zr are generally transported in ferromagnesian minerals, quartz, heavy minerals and clays (Armstrong-Altrin et al., 2004; Rahman and Suzuki, 2007). Heavy minerals like tourmaline and thorite, which have the detrital origin for Th, were not seen in this deposit. A strong correlation coefficient has been observed between Al_2O_3 and TiO_2 (>0.85), Al_2O_3 and Fe_2O_3 (>0.91), and Al_2O_3 and K_2O (>0.93) (see appendix 4, Fig. 8). This is consistent with the findings of the Khormuj samples (Haddad et al., 2023), suggesting an increase in these elements attributable to the rising detritus component within the Pabdeh Formation.. Nevertheless, a positive correlation exists between P_2O_5 with some elements such as MgO, Na_2O, U, Y (appendix 5, Fig. 8) and the REE (Fig. 11) in both of the deposits.

Apatite precipitation can occur directly from seawater P_2O_5, and the positive correlation between P_2O_5 and other elements indicates that they were also deposited with carbonate-phosphorite materials from seawater (Fig. 8). Cation replacement in apatite as a mechanism for trace metal enrichment and we test this hypothesis by examining the correlation between the

essential structural constituents of apatite (mainly CaO and P_2O_5) and other elements that have a positive correlation with these elements. Calcium is distributed in addition to carbonate fluorapatite between biogenic carbonates and detrital minerals. Marine sedimentary phosphate samples of Kangan anticline have ~0.34–11.11 wt.% P_2O_5 with the average concentration of 4.11 wt.% (Khormuj anticline phosphatic horizons P_2O_5 0.40–10.59 wt.%, average: 5.56 wt.%; Haddad et al., 2023). A positive correlation exists between Na_2O and P_2O_5 in the Pabdeh formation's phosphate samples (Fig. 8) which indicates the substitution of Na^+ for Ca^{2+} in francolite (Jiang et al., 2020). Between Y (appendix 5 and Fig. 8, r= 0.94) and REEs (Fig. 11, r = 0.60) also has a positive correlation with P_2O_5, indicating that these elements substituted for Ca in the carbonate fluorapatite structure. Unlike Khormuj phosphate samples, the studied samples do not have a strong positive good correlation between U with P_2O_5 with correlation coefficient 0.15 (Fig.8 and appendix 5). Similar to Khormuj phosphate samples, REEs positively correlate with P_2O_5 (Fig. 11) in the phosphate samples. Phosphate horizons are moderately enriched in the REE contrasted with the limestone and pelagic limestone horizons. Due to the positive correlation between REE and P_2O_5 (Fig. 11) in the Pabdeh Formation phosphate units and, lack of no U- or REE-rich minerals except for the carbonate fluorapatite in our samples in thin sections or through XRD, FE-SEM and SEM-EDX, it can be concluded that carbonate fluorapatite is most likely the main REE-bearing minerals in the Kangan deposit. Despite the Khormuj deposit where carbonate fluorapatite is the main U-bearing and REEs mineral, in the Kangan phosphate deposit, carbonate fluorapatite is not the main U-bearing mineral. Instead, it seems that adsorption of uranium by clay minerals and organic matter also plays a role.

The correlation between Y anomaly and $(La/Nd)_N$ ratio (Fig. 14) can be used to express post-depositional variations, as these parameters are not affected by changes in redox conditions (Molnar et al., 2018; Kechiched et al., 2020).

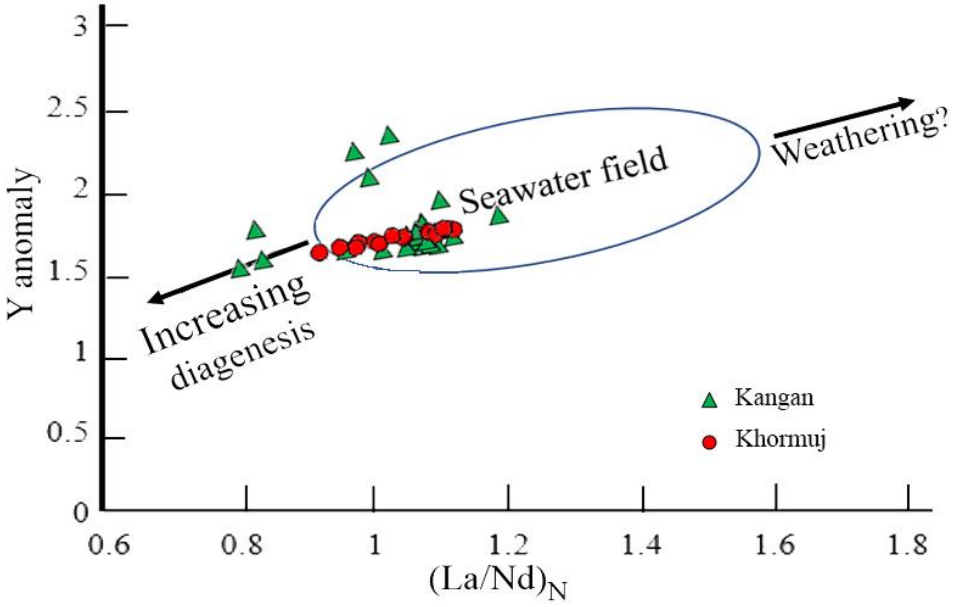

Figure 14. The binary diagram of Y anomaly versus $(La/Nd)_N$ for the studied phosphate samples in the Khormuj and Kangan anticlines (modified after Molnar et al. 2018; Kechiched et al. 2020).

Fig. 14, shows that the plotted phosphate samples from the Kangan (this study) and Khormuj (Haddad et al., 2023) anticlines fall within the range of seawater, although the values of some Kangan samples lie within the field of mild diagenesis. The sedimentary phosphate deposit of the Kangan anticline has been slightly affected by diagenesis compared to the deposit in the Khormuj anticline (Fig. 14). This suggests that the primary diagenetic processes have influenced the concentration of uranium. Consequently, the direct relationship between P_2O_5 and U has been disrupted, leading to the scattering of the uranium element. Between the upper and lower sections of the phosphatic and pelagic limestone layers in the Pabdeh Formation, variations in U concentrations exist. Samples from the lower part of phosphatic sedimentary layers (Ka12- Ka21-

Ka23- Ka33- Ka34) and from pelagic limestone layers (samples Ka1- Ka9- Ka19- Ka29) are more enriched in U than the samples taken from the upper layers. A possible reason for these higher concentrations of U is supergene enrichment. During supergene enrichment, U^{6+} is released and leached from the oxidized (due to weathering) upper layers, then deposited in the lower phosphate and pelagic limestone layers. The presence of organic matter, reduced environment, and surface adsorption in pelagic limestone layers would create a relatively reducing environment that would facilitate U deposition. In the effect of the oxidized water penetration into the sulfide-bearing units and reacted with pyrite, an acidic environment is obtained by producing H^+ and SO_4^{2-} ions. SO_4^{2-} is reacted with Ca^{2+} and provided gypsum. As a result of this acidic (as a result of H^+ ion) and oxidizing environment, uranium can remove from the phosphate layers either from the dissolution of apatite or from the dissolution of uranium on the surface sorption on the minerals, especially clay minerals and organic matter in phosphatic and pelagic limestone layers. Due to the U^{6+}-enriched fluid transition via the phosphatic layers and its gradual reduction, fine-grained uranium minerals (e.g., Baturin and Kochenov, 2001) or U substitution into phosphate minerals would deposit. Insomuch fine-grained U-rich minerals are not present there, it can be concluded that adsorption and substituting the phosphate minerals in phosphates from the Pabdeh Formation were U enrichment process.

5.3 Genetic model for phosphate deposition

The Cretaceous–Tertiary Pabdeh formation is exposed across the Zagros Fold Belt in southern Iran (Alipour, 2024) in several anticlines, including the Khormuj anticline (Haddad et al., 2023) and the Kangan anticline (this study). Both have similar stratigraphy and have whole-rock compositions that suggest REE and U substitution into phosphate minerals and not ion substitution.

An integrated genetic model (Fig. 15) for the deposition phosphate layers rich in elements of economic interest in the Pabdeh Formation of the Kangan and Khormuj anticlines is presented. This model fuses observations and inferences about the paleodepositional environment and host minerals of trace metals.

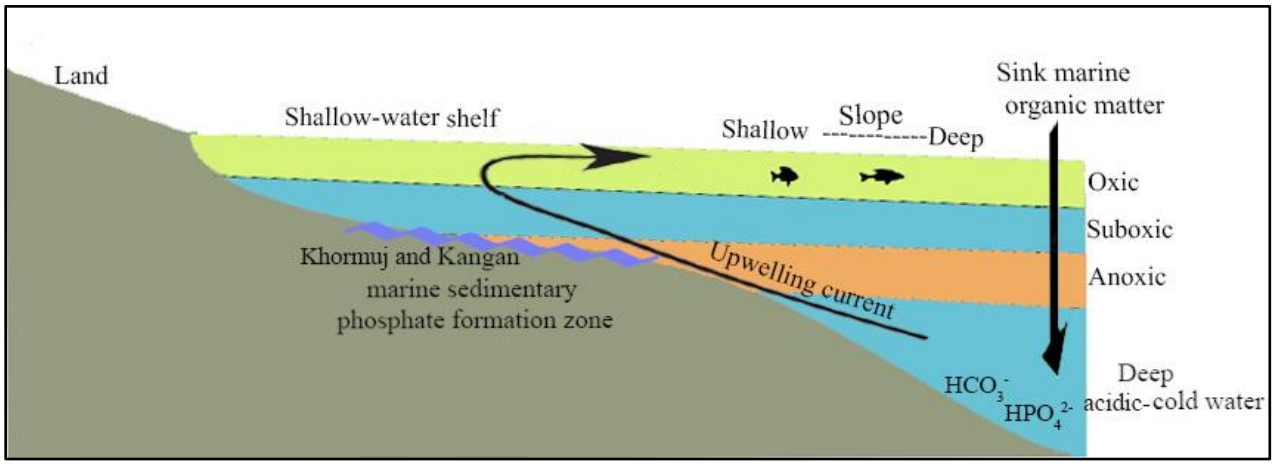

Figure 15. A genetic model for the deposition phosphate layers in the Pabdeh Formation of the Kangan and Khormuj anticline

The pelagic limestone layers beneath lower limestone layers with mudstone textures microfractures have rare bioclasts, significant pelagic foraminifera (such as Globigerinas and Globorotalias), strong laminations and do not contain glauconite. These textures and the presence of plankton suggest sediment deposition below the open ocean photic zone in a moderately low-energy and deep depositional environment; the pelagic limestone layers are covered by carbonate with the sharp boundary.

The limestone layers probably formed as a result of the transgression. Having pelagic foraminifera in the open sea suggests that these microfacies were formed in an outer ramp environment with a deep depositional environment and relatively low energy.

Due to seawater regression, upwelling currents and deep cold acidic seawater movement enriched with organic matter, HCO_3^- and HPO_4^{2-} ions towards the continental shelf, sandy glauconite-bearing phosphate layers with grainstone textures of the Pabdeh Formation were deposited in a relatively shallow, turbulent and energetic environment. As a result of K^+ enriched seawater and pore waters, simultaneously with phosphatic layers deposition in the Pabdeh Formation of the Kangan and Khormuj anticlines, primary and secondary glauconites were precipitated.

As a result of re-transgression, in an environment with lower energy and greater depth in the offshore basin formation related to the open sea, the upper limestone layers with wackstone to packstone carbonate texture, comprising planktonic foraminifera, were deposited in the micrite matrix. Nodules with various sizes are phosphatic pieces separated from phosphatic layers then rounded by turbidity currents distributed throughout the lower and upper limestone layers. Due to the greater depth of formation environment, the paleoredox conditions, and the absence of phosphatization process, in the time formation of limestone layers, organic matter has been finely preserved in them. Negative Ce anomalies and slight positive Eu anomalies are in normalized REE patterns of Pabdeh Formation phosphate samples in Kangan and Khormuj anticlines; it suggested phosphate precipitation in a relatively oxidized situation (Zarasvandi et al., 2021). The REEs pattern was also shown slightly enriched in HREEs (Fig. 12) and enriched in MREEs (Fig. 12 and Fig. 13) in the phosphates of the Pabdeh Formation.

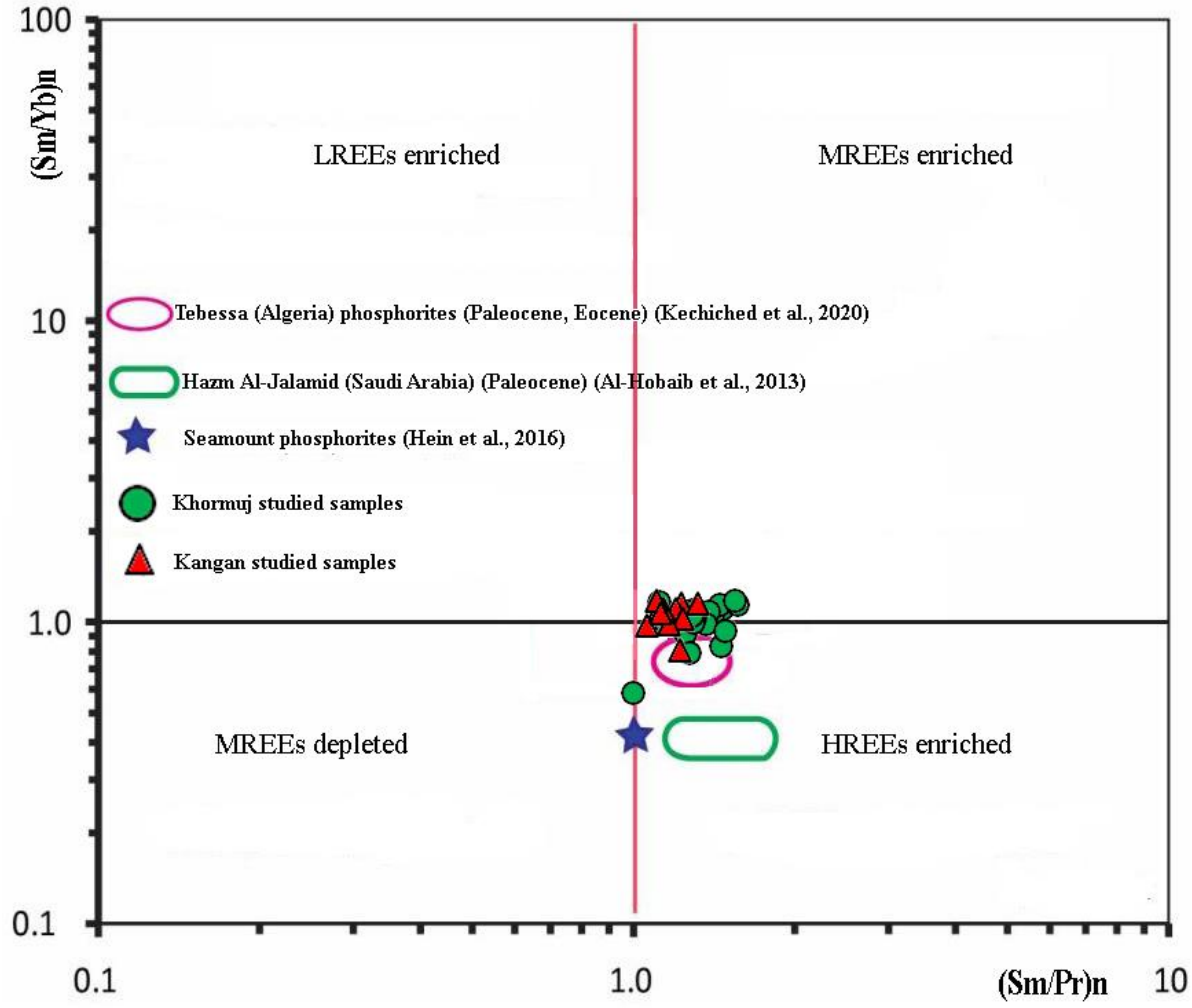

Figure 13. Plotting the relationship between (Sm/Pr)n and (Sm/Yb)n in the samples studied in the Kangan sections Khormuj (Haddad et al., 2023) and comparing them with other phosphates (modified from Sasmaz et al., 2023).

Significant fractionation between the LREEs and the HREEs in both of the deposits occurred; this is indicated by the low $(\Sigma LREE/\Sigma HREE)_N$ ratios of the Pabdeh Formation phosphate samples.

The samples of Pabdeh Formation marine sedimentary phosphatic layers of the Kangan anticline show uranium enrichment and thorium depletion (Fig. 10a). As a result of the supergene enrichment, more U enrichment has been occurred in the lower part of these marine sedimentary

phosphatic layers than in the upper portions. Francolite is probably the dominant host of the U and REE because no minerals with essential structural components of uranium or the REEs were observed in samples. Rare earth element-rich phosphate deposits are controlled by the depositional environment because, during precipitation, trace amounts of Na_2O, Cr, U, Sr, Th, REEs, and Y were partitioned. As a result of this partitioning, economic interest trace metals were enriched.

In the samples from the Pabdeh Formation of the Khormuj anticline (Haddad et al., 2023), the Th/U ratios range from 0.1 to 0.94, while in the Kangan anticline, the ratio ranges from 0.05 to 1.16 (Appendix 3). The Th/U ratio can be utilized to determine the environmental conditions prevalent during the formation of the marine sedimentary phosphate deposit. According to Molnar et al. (2018), a Th/U ratio of less than 2 signifies an anoxic environment, while a ratio greater than 7 indicates an oxic one, and a ratio in the range of 2 to 7 suggests a suboxic environment. The Th/U ratio in the phosphate samples of the Pabdeh Formation of the Khormuj anticline indicates formation in a suboxic to anoxic environment under reducing conditions, while the Th/U ratio in the sample from the Kangan anticline signals formation in an anoxic environment. Contrary to expectations, the Khormuj anticline sedimentary phosphate deposit exhibits higher U concentrations than the Kangan anticline deposit, potentially attributed to reduced inflow of U^{6+} ions from the continent to the ocean by the river during the formation of the Kangan anticline marine sedimentary deposit (Fig. 10b). This lower U input could be due to several factors, including the low concentration of uranium in weathered continental mother rocks, low chemical weathering in continental parent rocks, and the presence of a reducing environment along the river before entering the sedimentary basin. Despite the more suitable sedimentary environment for uranium deposition at the Kangan anticline, higher U concentrations are observed in the Khormuj anticline (Fig. 10b).

The Pabdeh formation's sedimentary marine phosphate of the Kangan anticline is potentially a large resource of the REE and uranium. The enrichment of these elements relative to other chemical sedimentary rocks is due to appropriate ocean and deposition conditions for phosphate mineralization. Phosphate-rich horizons that experienced similar deposition conditions to the Pabdeh formation are important exploration targets for REE and U mineralization. Given the current mining technologies, the Khormuj and Kangan deposits are not economically viable at the moment. However, with the continued progress of science and technology, these deposits may have the potential to be exploited for the extraction of uranium (U) and rare earth elements (REE) in the future.

6. Conclusions

Marine phosphate deposit of Kangan anticline Pabdeh formation (Early Eocene- Middle Eocene) were deposited in carbonate host rock in the stable carbonate ramp connected to the open ocean. These deposits are enriched in trace metals of economic interest, such as U and the HREE. Phosphorus grainstone–packstone with microfossils and green glauconite are present in the phosphatic layer. The phosphate whole-rock chemical analysis shows they had a minimal detrital component and were enriched in U and HREEs compared with carbonate layers. As a result of interpreting phosphate layers textures and trace element compositions could be suggested a basin margin carbonate ramp for formation environment with the reduced and suboxic-to-anoxic situation and low detrital input but occasionally high-energy erosional events. Negative correlation between P_2O_5 and U in this deposit suggests that absorption in clay minerals is the main mechanism for U enrichment. Positive correlations between P_2O_5 and REEs in this deposit suggest cation substitution into carbonate fluorapatite structures is the main metal enrichment mechanism.

Moderately enrichment of HREEs related to their marine origin is evident. Phosphate layers have REEs patterns that exhibit low $((\Sigma LREE/\Sigma HREE)_N)$ ratios and strong negative Ce anomalies.

Declaration of Competing Interest

The authors declare that they have no known competing financial interests or personal relationships that could have appeared to influence the work reported in this paper.

Acknowledgements

This research was performed with the support of the Faculty of Earth Sciences at Shahid Beheshti University, the Applied Research Center of the Geological Survey of Iran (Karaj), and the Iranian Atomic Energy Organization. We appreciate Dr. Chris Yakymchuk for his generous help in writing our research. We also thank the two reviewers for their constructive comments on this manuscript.

References

Abdulnaby, W., 2019. Chapter 4–Structural Geology and Neotectonics of Iraq, Northwest Zagros. Developments in Structural Geology and Tectonics. Vol. 3. https://doi.org/10.1016/B978-0-12-815048-1.00004-4

Abed, A.M., 2013. The eastern Mediterranean phosphorite giants: an interplay between tectonics and upwelling. GeoArabia 18, 67-94. https://doi.org/10.2113/geoarabia180267.

Abed, A.M., Jaber, O., Alkuisi, M., Sadaqah, R., 2016. Rare earth elements and uranium geochemistry in the Al-Kora phosphorite province, Late Cretaceous, northwestern Jordan. Arabian Journal of Geosciences 9, 187. https://doi.org/10.1007/s12517-015-2135-6.

Adams, A.E., MacKenzie, W.S., Guilford, C., 2017. Atlas of sedimentary rocks under the microscope. Routledge. 10.1180/minmag.1985.049.350.27.

Adepoju, S. A., Ojo, O. J., Akande, S. O., Sreenivas, B., 2021. Petrographic and geochemical constraints on petrofacies, provenance and tectonic setting of the upper cretaceous

sandstones, Northern Bida Basin, north-central Nigeria. Journal of African Earth Sciences, 174, 104041. https://doi.org/10.1016/j.jafrearsci.2020.104041.

Aghanabati, A., 2004. Geology of Iran. Geology and Mineral Exploration Organization of the country, The first edition, p 30-60 (in persian).

Ahifar, A., Kani, A., AMIRI, B.H., 2015. Limestone nanofossil biostratigraphy of Pabdeh Formation at Gurpi anticline. 10.22071/GSJ.2015.42301.

Alipour, M., 2024. Petroleum systems of the Iranian Zagros Fold and Thrust Belt. Results in Earth Sciences 2,100027. https://doi.org/10.1016/j.rines.2024.100027

Armstrong-Altrin, J. S., Lee, Y. I., Verma, S. P., Ramasamy, S., 2004. Geochemistry of sandstones from the upper Miocene Kudankulam Formation, southern India: Implications for provenance, weathering, and tectonic setting. Journal of sedimentary Research, 74(2), 285-297. https://doi.org/10.1306/082803740285.

Arning, E.T., Lückge, A., Breuer, l.C., Gussone, N., Birgel, D., Peckmann, J., 2009. Genesis of phosphorite crusts off Peru. Marine Geology 262, 68-81. https://doi.org/10.1016/j.margeo.2009.03.006.

Avilés, A., Rodero, J., Amores, V., De Vicente, I., Rodríguez, M.I., Niell, F.X., 2006. Factors controlling phosphorus speciation in a Mediterranean basin (River Guadalfeo, Spain). Journal of Hydrology 331, 396-408. https://doi.org/10.1016/j.jhydrol.2006.05.024.

Baioumy, H., 2002. Forms of iron in the phosphorites of Abu-Tartur area, Egypt. Chinese journal of geochemistry 21, 215-226. 10.1007/BF02831086.

Baioumy, H., 2011. Rare earth elements and sulfur and strontium isotopes of upper Cretaceous phosphorites in Egypt. Cretaceous Research 32, 368-377. https://doi.org/10.1016/j.cretres.2011.01.008.

Baldermann, A., Warr, L. N., Letofsky-Papst, I., Mavromatis, V., 2015. Substantial iron sequestration during green-clay authigenesis in modern deep-sea sediments. Nature Geoscience, 8(11), 885-889. https://doi.org/10.1038/ngeo2542.

Balthasar, U., 2007. An Early Cambrian organophosphatic brachiopod with calcitic granules. Palaeontology 50, 1319-1325. https://doi.org/10.1111/j.1475-4983.2007.00729.x.

Banerjee, S., Chattoraj, S. L., Saraswati, P. K., Dasgupta, S., Sarkar, U., 2012. Substrate control on formation and maturation of glauconites in the Middle Eocene Harudi Formation,

western Kutch, India. Marine and Petroleum Geology, 30(1), 144-160. https://doi.org/10.1016/j.marpetgeo.2011.10.008.

Baturin, G., Kochenov, A., 2001. Uranium in phosphorites. Lithology and mineral resources 36, 303-321. https://doi.org/10.1023/A:1010406103447.

Benitez-Nelson, C., O'Neill, L., Kolowith, L.C., Pellechia, P., Thunell, R., 2004. Phosphonates and particulate organic phosphorus cycling in an anoxic marine basin. Limnology and Oceanography 49, 1593-1604. https://doi.org/10.4319/lo.2004.49.5.1593.

Boggs, S., 2014. Principles of Sedimentology and Stratigraphy (5th ed.). Pearson. ISBN-13: 9780321643186.

Bolourchifard, F., Fayazi, F., Mehrabi, B., Memarkouchehbagh, A., 2019. Evidence of high-energy storm and shallow water facies in Pabdeh sedimentary phosphate deposit, Kuhe-Lar-anticline, SW Iran. Carbonates and Evaporites 34, 1703-1721. https://doi.org/10.1007/s13146-019-00520-4.

Brandano, M., Westphal, H., Mateu-Vicens, G., Preto, N., Obrador, A., 2016. Ancient upwelling record in a phosphate hardground (Tortonian of Menorca, Balearic Islands, Spain). Marine and Petroleum Geology, 78, 593-605. https://doi.org/10.1016/j.marpetgeo.2016.07.017.

British Geological Survey, 2011. Rare Earth Elements Mineral Profile. Centre for Sustainable Mineral Development, p. 54.

Brookfield, M., Hemmings, D., Van Straaten, P., 2009. Paleoenvironments and origin of the sedimentary phosphorites of the Napo Formation (Late Cretaceous, Oriente Basin, Ecuador). Journal of South American Earth Sciences 28, 180-192. https://doi.org/10.1016/j.jsames.2009.02.004.

Chen, J., Zhang, J., Yang, R., 2010. Mode of occurrence of rare earth elements in phosphorite in Zhijin county, Guizhou province, China. Acta Mineral. Sin 30, 123-129. (In Chinese with English abstract)

Christmann, P., 2014. A forward look into rare earth supply and demand: A role for sedimentary phosphate deposits? Procedia Eng., 83, 19–26. https://doi.org/10.1016/j.proeng.2014.09.005.

Collins, L. B., James, N. P., Bone, Y., 2014. Carbonate shelf sediments of the western continental margin of Australia. Geological Society, London, Memoirs, 41(1), 255-272. https://doi.org/10.1144/M41.19.

Condie, K.C., 1993. Chemical composition and evolution of the upper continental crust: contrasting results from surface samples and shales. Chemical Geology 104: 1-37. 10.1016/0009-2541(93)90140-E.

Dahlkamp, F.J., 1993. Uranium ore deposits. Springer-Verlag, Berlin, Heidelberg, New York. 10.1007/978-3-662-02892-6

Dahlkamp, F.J., 2009. Uranium Deposits of the World: Uranium in Asia–Overview- Part II. vol. 1. Springer-Verlag, Berlin, Heidelberg. 10.1007/978-3-540-78558-3_19

Daessle, L. W., Carriquiry, J. D. 2008. Rare earth and metal geochemistry of Land and Submarine phosphorites in the Baja California Peninsula, Mexico. Marine Georesources and Geotechnology, 26(4), 340-349. https://doi.org/10.1080/10641190802382633.

Dar, S. A. 2013. Geochemical and Mineralogical studies of Phosphorites and Associated rocks in parts of Lalitpur district, Uttar Pradesh, India. Ph. D. Thesis (Unpublished), Department of Geology, Aligarh Muslim University, Aligarh, pp. 35-54. http://hdl.handle.net/10603/182923.

Doner, H.E., and W.C. Lynn. 1977. Carbonate, halide, sulfate, and sulfide minerals. In: J.B. Dixon and S.B. Weed (eds.), Minerals in Soil Environments. Soil Science Society of America, Madison, Wisconsin. 75–98. https://doi.org/10.2136/sssabookser1.2ed.c6.

Emsbo, P., McLaughlin, P.I., Breit, G.N., du Bray, E.A., Koenig, A.E., 2015. Rare earth elements in sedimentary phosphate deposits: solution to the global REE crisis? Gondwana Research 27, 776-785. http://dx.doi.org/10.1016/j.gr.2014.10.008.

Fazio, A.M., Scasso, R.A., Castro, L.N., Carey, S., 2007. Geochemistry of rare earth elements in early-diagenetic miocene phosphatic concretions of Patagonia, Argentina: Phosphogenetic implications. Deep Sea Research Part II: Topical Studies in Oceanography 54, 1414-1432. https://doi.org/10.1016/j.dsr2.2007.04.013.

Felitsyn, S., Morad, S., 2002. REE patterns in latest Neoproterozoic–early Cambrian phosphate concretions and associated organic matter. Chemical Geology 187, 257-265. https://doi.org/10.1016/S0009-2541(02)00046-3.

"File: ZagrosFTB.png." Wikimedia Commons. 18 Jan 2022, 01:23 UTC. 12 Mar 2024, 23:39 <https://commons.wikimedia.org/w/index.php?title=File:ZagrosFTB.png&oldid=622433488>.

Flügel, E., Munnecke, A., 2010. Microfacies of carbonate rocks: analysis, interpretation and application. (Vol. 976, p. 2004). Berlin: Springer. https://doi.org/10.1007/978-3-642-03796-2.

Flugel, E., 2004. Microfacies of carbonate rocks: analysis, interpretation and application. Springer Science & Business Media. 10.1017/S0016756806221940.

Gál, P., Polgári, M., Józsa, S., Gyollai, I., Kovács, I., Szabó, M., Fintor, K., 2020. Contribution to the origin of Mn-U-Be-HREE-enrichment in phosphorite, near Bükkszentkereszt, NE Hungary. Ore Geology Reviews 125, 103665. https://doi.org/10.1016/j.oregeorev.2020.103665.

Gong, M.L., 2007. Phase Analysis and Geological Prospecting, 2nd ed. Geological Publishing House: Beijing, China, pp. 161–172.

Gueguin, M. and Cardarelli, F., 2007. Chemistry and mineralogy of titania-rich slags. Part 1—Hemo-ilmenite, sulphate, and upgraded titania slags. Mineral Processing and Extractive Metallurgy Review, 28, 1-58. https://doi.org/10.1080/08827500600564242.

Hadavi, F., Saboot, M., 2012. Nanostratigraphy of the boundary of Gurpi Pabdeh formations in the Tang-e-Dorahak section (south of Kangan anticline) 16th Symposium of Geological Society of Iran،Shiraz (in persian).

Haddad, F., Yazdi, M., Behzadi, M., Yakymchuk, C. and Khoshnoodi, K., 2023. Mineralogy, geochemistry, and depositional environment of phosphates in the Pabdeh Formation, Khormuj anticline, SW of Iran. Environmental Earth Sciences, 82(18), p.418. https://doi.org/10.1007/s12665-023-11090-z

Haddad, F., Yazdi, M., Behzadi, M., Khoshnoudi, K., 2020. Mineralogical and geological features of phosphates mineralization in Pabdeh-Gurpi Formation, Kangan anticline, SW of Iran. The 23rd Symposium of Geological Society of Iran (in persian).

Hannigan, R. E., Sholkovitz E. R., 2001. "The development of middle rare earth element enrichments in freshwaters: weathering of phosphate minerals." Chemical Geology 175.3-4: 495-508. https://doi.org/10.1016/S0009-2541(00)00355-7.

Harding, S.C., Nash, B.P., Petersen, E.U., Ekdale, A., Bradbury, C.D., Dyar, M.D., 2014. Mineralogy and geochemistry of the Main Glauconite Bed in the Middle Eocene of Texas: Paleoenvironmental implications for the Verdine Facies. PloS one 9, e87656. https://doi.org/10.1371/journal.pone.0087656.

Hein, J.R., Koschinsky, A., Mikesell, M., Mizell, K., Glenn, C.R., Wood, R., 2016. Marine Phosphorites as Potential Resources for Heavy Rare Earth Elements and Yttrium. Minerals 6, 88. https://doi.org/10.3390/min6030088.

Heydari, E., 2008. Tectonics versus eustatic control on supersequences of the Zagros Mountains of Iran. Tectonophysics 451, 56-70. https://doi.org/10.1016/j.tecto.2007.11.046.

Hiatt, E. E., Pufahl, P. K., Edwards, C. T., 2015. Sedimentary phosphate and associated fossil bacteria in a Paleoproterozoic tidal flat in the 1.85 Ga Michigamme Formation, Michigan, USA. Sedimentary Geology, 319, 24-39. https://doi.org/10.1016/j.sedgeo.2015.01.006.

Hughes, J.M., Rakovan, J., 2018. 1. The Crystal Structure of Apatite, Ca_5 (PO_4) $_3$ (F, OH, Cl). Phosphates, 1-12. https://doi.org/10.1515/9781501509636-004.

Hughes, J.M., Rakovan, J.F., 2015. Structurally robust, chemically diverse: apatite and apatite supergroup minerals. Elements 11, 165-170. https://doi.org/10.2113/gselements.11.3.165.

Humphries, M., 2010. Rare earth elements: the global supply chain. CRS Report for Congress, p. 27.

Ismael, I. S. 2002. Rare earth elements in Egyptian phosphorites. Chinese journal of geochemistry, 21(1), 19-28. https://doi.org/10.1007/BF02838049.

James, N. P., Bone, Y., Kyser, T. K., Dix, G. R., Collins, L. B., 2004. The importance of changing oceanography in controlling late Quaternary carbonate sedimentation on a high-energy, tropical, oceanic ramp: north-western Australia. Sedimentology, 51(6), 1179-1205.

https://doi.org/10.1111/j.1365-3091.2004.00666.x.

Jasinski, S. M., 2011. Phosphate rock. In Mineral Commodity Summaries 2011, US Geological Survey, United States Government Printing Office, Washington, D.C.

Jiang, X.D., Sun, X.M., Chou, Y.M., Hein, J.R., He, G.W., Fu, Y., Li, D.F., Liao, J.L. Ren, J.B., 2020. "Geochemistry and origins of carbonate fluorapatite in seamount Fe-Mn crusts from the Pacific Ocean." Marine Geology 423: 106135. https://doi.org/10.1016/j.margeo.2020.106135.

Jiménez-Millán, J., Castro, J. M., 2008. K-feldspar alteration to gel material and crystallization of glauconitic peloids with berthierine in Cretaceous marine sediments—sedimentary

implications (Prebetic Zone, Betic Cordillera, SE Spain). Geological Journal, 43(1), 19-31. https://doi.org/10.1002/gj.1093.

Kato, Y., Fujinaga, K., Nakamura, K., Takaya, Y., Kitamura, K., Ohta, J., Toda, R., Nakashima,T., Iwamori, H., 2011. Deep-sea mud in the Pacific Ocean as a potential resource for rare-earth elements. Nature Geoscience 4, 535–539. https://doi.org/10.1038/ngeo1185.

Khoshnoodi, K. and Ziapour, S., 2022. Uranium and rare earth elements in the phosphate deposits of the Pabdeh Formation, Zagros Zone, Iran: concentrations and geochemical patterns comparison. Environmental Earth Sciences, 81(14), p.362. 10.1007/s12665-022-10488-5

Liu, T., Hu, Y., Chen, N., Ma, L., He, Q., Feng, C., 2020. Microbial redox activity mediated anaerobic pyrite oxidation under circumneutral conditions. bioRxiv. 10.1016/j.jhazmat.2021.125844.

Liu, X.T., Li, A.C., Dong, J., Zhuang, G.C., Xu, F.J., Wan, S.M., 2018c. Nonevaporative origin for gypsum in mud sediments from the East China Sea shelf. Marine Chemistry. 205, 90-97. https://doi.org/10.1016/j.marchem.2018.08.009.

Long, D. T., Krantz, R. W., Depetris, P. J., Shaw, R. D., and Ladd, D. M. 2011. Sedimentology, paleoecology, and source rock potential of phosphate-rich carbonate rocks from the lower Miocene Kailas and upper Oligocene to middle Miocene Sagaing Formations, Chindwin Basin, Sagaing Division, Myanmar (Burma). American Association of Petroleum Geologists bulletin, 95(9), 1515-1537.

Long, K.R., Van Gosen, B.S., Foley, N.K., Cordier, D., 2010. The principal rare earth elements deposits of the United States—a summary of domestic deposits and a global perspective. U.S. Geological Survey Scientific Investigations Report 2010–5220. 10.1007/978-90-481-8679-2_7.

McLennan SM, 1989. Rare earth elements in sedimentary rocks: influence of provenance and sedimentary processes. Geochemistry and mineralogy of rare earth elements, pp169-200. https://doi.org/10.1515/9781501509032-010

Mercadier, J., Cuney, M., Lach, P., Boiron, M.C., Bonhoure, J., Richard, A., Leisen, M. and Kister, P., 2011. Origin of uranium deposits revealed by their rare earth element signature. Terra Nova, 23(4), 264-269. https://doi.org/10.1111/j.1365-3121.2011.01008.x

Messadi, A. M., Mardassi, B., Ouali, J. A., Touir, J., 2019. Phosphate genesis and concentration a response to sea level fluctuation in shallow marine environments of the lower Eocene deposits in the southern Tethyan margin: case study of the Gafsa Basin, southern Tunisia. Carbonates and Evaporites, 34(4), 1489-1509. https://doi.org/10.1007/s13146-019-00498-z.

Molnár, Z., Kiss, G., Dunkl, I., Czuppon, G., Zaccarini, F., Dódony, I. 2018. Geochemical characteristics of Triassic and Cretaceous phosphorite horizons from the Transdanubian Mountain Range (western Hungary): Genetic implications. Mineralogical Magazine, 82(S1), S147-S171. 10.1180/minmag.2017.081.103

Motiei, H., 2003. Geology of Iran: Stratigraphy of Zagros. A Publication of the Geological Survey of Iran, 536 pp. (in Persian). Association of Petrology Geology Bullten 49:2182–2245.

Mutti, M., Bernoulli, D., 2003. Early marine lithification and hardground development on a Miocene ramp (Maiella, Italy): key surfaces to track changes in trophic resources in nontropical carbonate settings. Journal of Sedimentary Research, 73(2), 296-308. https://doi.org/10.1306/083102730296.

Nasrollahzadeh Saravi, H., Pouraria, A., Nowruzi, B., 2015. Phosphorus forms of the surface sediment in the Iranian coast of the Southern Caspian Sea. Caspian Journal of Environmental Sciences 13, 141-151.

Nichols, G. (2009) Sedimentology and Stratigraphy. 2nd Edition, Wiley-Blackwell, Hoboken. ISBN 978-1-4051-3592-4 Odin, G. S. and Letolle, R., 1980. Glauconitization and phosphatization environments: a tentative comparison. In: Y. K. Bentor (Editor), Marine Phosphorites, Society of Economic Paleontologists and Mineralogists Special Publication, 29, 227-238. https://doi.org/10.2110/pec.80.29.0227.

Pestitschek, B., Gier, S., Essa, M., Kurzweil, H., 2012. Effects of weathering on glauconite: evidence from the Abu Tartur Plateau, Egypt. Clays and clay minerals 60, 76-88. 10.1346/CCMN.2012.0600107

Pirlet, H., Wehrmann, L. M., Brunner, B., Frank, N., Dewanckele, J. A. N., Van Rooij, D., Henriet, J. P., 2010. Diagenetic formation of gypsum and dolomite in a cold-water coral mound in the Porcupine Seabight, off Ireland. Sedimentology, 57(3), 786-805.

https://doi.org/10.1111/j.1365-3091.2009.01119.x.

Picard, S., Lécuyer, C., Barrat, J.-A., Garcia, J.-P., Dromart, G., Sheppard, S.M.F., 2002. Rare earth element contents of Jurassic fish and reptile teeth and their potential relation to seawater composition (Anglo-Paris Basin, France and England). Chemical Geology 186, 1–16. https://doi.org/10.1016/S0009-2541(01)00424-7.

Pufahl, P.K., Pirajno, F., Hiatt, E.E., 2013. Riverine mixing and fluvial iron formation: A new type of Precambrian biochemical sediment. Geology 41, 1235-1238. https://doi.org/10.1130/G34812.1.

Rahman, M. J. J., Suzuki, S., 2007. Geochemistry of sandstones from the Miocene Surma Group, Bengal Basin, Bangladesh: Implications for Provenance, tectonic setting and weathering. Geochemical Journal, 41(6), 415-428. https://doi.org/10.2343/geochemj.41.415.

Rajabzadeh, M.A., Haddad, F., Polgári, M., Fintor, K., Walter, H., Molnár, Z., Gyollai, I., 2017. Investigation on the role of microorganisms in manganese mineralization from Abadeh-Tashk area, Fars Province, southwestern Iran by using petrographic and geochemical data. Ore Geology Reviews 80, 229-249. http://dx.doi.org/10.1016/j.oregeorev.2016.06.035

Rakovan, J. F., Hughes, J. M., 2000. Strontium in the apatite structure: strontian fluorapatite and belovite-(Ce). The Canadian Mineralogist, 38(4), 839-845. https://doi.org/10.2113/gscanmin.38.4.839.

Rezaei, F., Azizi, H., Asahara, Y., 2021. Tectonic significance of the late Eocene (Bartonian) calc-alkaline granitoid body in the Marivan area, Zagros suture zone, northwest Iran. International Geology Review, 1-16. https://doi.org/10.1080/00206814.2021.1907624.

Robb, L., 2020. Introduction to ore-forming processes. John Wiley and Sons.

Senemari, S., Foroghi, F., 2019. Limestone nannofossils biostratigraphy of the Campanian-Danian interval, Gurpi Formation in the Zagros Basin, SouthWest Iran. Geopersia 9, 251-264. 10.22059/GEOPE.2019.269957.648432.

Sanders, C., Grotzinger, J., 2021. Sedimentological and stratigraphic constraints on depositional environment for Ediacaran carbonate rocks of the São Francisco Craton: Implications for phosphogenesis and paleoecology. Precambrian Research, 363, 106328. https://doi.org/10.1016/j.precamres.2021.106328.

Sepehr, M., Cosgrove, J., 2004. Structural framework of the Zagros fold–thrust belt, Iran. Marine and Petroleum geology 21, 829-843. https://doi.org/10.1016/j.marpetgeo.2003.07.006.

Shields, G.A., Stille, P., 2001. Diagenetic constraints on the use of cerium anomalies as palaeoseawater redox proxies: an isotopic and REE study of Cambrian phosphorites. Chemical Geology 175, 29–48. https://doi.org/10.1016/S0009-2541(00)00362-4.

Simandl, G., Paradis, S., Fajber, R., 2011. Sedimentary phosphate deposits mineral deposit profile F07. Technical Report, British Columbia Ministry of Energy, Mines and Petroleum Resources 217–222.

Subbotina, N., 1947. Foraminifery datskikh i paleogenovykh otlozhenii severnogo Kavkaza [Foraminifera of the Danian and Paleogene deposits of the northern Caucasus]. Trudy Vesesoyuznogo Nauchno-Issledovatel'skogo Geologo-Razvedochnogo Neftyanogo Instituta, Novaya Seriya (VNIGNI), 39-160.

Tarawneh, K., 2005. New phosphorite deposits in Naqib Etaiq area (southeastern Jordan). annual of the university of mining and geology. Geology and Geophysics 48 Part I, 32-43.

Tostevin, R., Shields, G.A., Tarbuck, G.M., He, T., Clarkson, M.O., Wood, R.A., 2016. Effective use of cerium anomalies as a redox proxy in carbonate-dominated marine settings. Chemical Geology. 438, 146–162. https://doi.org/10.1016/j.chemgeo.2016.06.027.

Trela, W., 2005. Condensation and phosphatization of the Middle and Upper Ordovician limestones on the Malopolska Block (Poland): response to paleoceanographic conditions. Sedimentary Geology, 178(3-4), 219-236. https://doi.org/10.1016/j.sedgeo.2005.05.005.

Tucker, M. E., 2001. Sedimentary Petrology: An Introduction to the Origin of Sedimentary Rocks (3rd edition). Blackwell Science. ISBN: 978-1-118-69890-7

Tzifas, I. T., U. A. Glasmacher, P. Misaelides, A. Godelitsas, P. N. Gamaletsos, J. Goettlicher, and D. Françoso de Godoy, 2017. Uranium-bearing francolites present in organic-rich limestones of NW Greece: a preliminary study using synchrotron radiation and fission track techniques. Journal of radioanalytical and nuclear chemistry 311, no. 1: 465-472. https://doi.org/10.1007/s10967-016-4973-4.

Van Kauwenbergh, S.J., 2010. World phosphate rock reserves and resources. Technical Bulletin. International Fertilizer Development Center-T-75 Muscle Shoals.

Vika, E., Agustin, M.A., Antonio, S.N., 2004. Secondary processes in upper Jurassic glauconite of the west Siberia geosyneclise, 32nd International Geological Congress, Florence, Italy, August 20-28, 2004: Abstracts Volume.

Virtasalo, J.J., Löwemark, L., Papunen, H., Kotilainen, A.T. and Whitehouse, M.J., 2010. Pyritic and baritic burrows and microbial filaments in postglacial lacustrine clays in the northern Baltic Sea. Journal of the Geological Society, 167(6), pp.1185-1198. https://doi.org/10.1144/0016-76492010-017.

Voronin, M., 2019. Mossbauer spectroscopy of glauconite as a source of information about the redox conditions of sedimentation, The 4th International Scientific and Practical Conference Innovations in geology, geophysics and geography, p. 97.

Voyseh S., 2017. The prospecting report of rare earth elements in the sedimentary phosphate horizons of Iran, (Exploration of rare earth elements in Iran), (In Persian with English abstract), 218.

Weaver, C.E., Pollard, L.D., 1973. Developments in Sedimentology, The Chemistry of Clay Minerals. Elsevier Scientific Publishing Company 15, 1–213.

Worden, R. H., and Burley, S. D., 2003. Sandstone Diagenesis: The Evolution of Sand to Stone. In R. H. Worden and S. D. Burley (Eds.), Sandstone Diagenesis: Recent and Ancient (pp. 3-44). Blackwell Publishing. ISBN: 978-1-444-30446-6.

Zanin, Y. N., Zamirailova, A. G. 2007. Trace elements in supergene phosphorites. Geochemistry International, 45(8), 758-769. 10.1134/S001670290701003X.

Zarasvandi, A., Fereydouni, Z., Alizadeh, B., Absar, N., Shukla, A.D., Raza, M.Q., Ashok, M. and Zentilli, M., 2021. Phosphogenesis in the Zagros Fold-Thrust Belt, Iran: The link between the Tethyan paleoenvironment and phosphate ore deposition. Ore Geology Reviews, 139, 104563. https://doi.org/10.1016/j.oregeorev.2021.104563.

Zeebe, R.E., 2012. History of seawater carbonate chemistry, atmospheric CO_2, and ocean acidification. Annual Review of Earth and Planetary Sciences 40. 10.1146/annurev-earth-042711-105521.

Zhang, Z., Jiang, Y., Niu, H., Xing, J., Yan, S., Li, A., Weng, Q. and Zhao, X., 2021. Enrichment of rare earth elements in the early Cambrian Zhijin phosphorite deposit, SW China: Evidence from francolite micro-petrography and geochemistry. Ore Geology Reviews, 138, 104342.Zhu, B., Jiang, S.Y., 2017. A LA-ICP-MS analysis of rare earth

elements on phosphatic grains of the Ediacaran Doushantuo phosphorite at Weng'an, South China: implication for depositional conditions and diagenetic processes. Geological Magazine 154, 1381-1397. 10.1017/S001675681700022X